Hotspots and Drivers: Locating Critical Groundwater Storage Watersheds and Their Dominant Factors

Özlem Baydaroğlu[1,*], Serhan Yeşilköy[1]

[1] Graduate School of Informatics, Middle East Technical University, Ankara, Türkiye

[*]Corresponding author: Özlem Baydaroğlu, ozlemby@metu.edu.tr

Abstract

Groundwater is a vital freshwater resource, and groundwater storage (GWS) is a key indicator of its resilience. This study identifies the watersheds of Türkiye with the most critical GWS conditions and the factors that dominate GWS variability in each of them. GWS, precipitation, and evapotranspiration (ET) data of 25 watersheds (October 2003 – September 2024) are used to train a Graph WaveNet (GWN) model that predicts GWS anomalies six months ahead. On the independent test period, pooled over all watersheds, it reproduces the temporal pattern of the anomalies ($r = 0.75$) but overestimates their level (bias = +48 mm; NSE = −0.23). The model serves as the basis for the attribution analysis. Explainable artificial intelligence (XAI; GradientSHAP) attributes the predictions to GWS history, precipitation, and ET: GWS memory dominates in all watersheds (58–74% of the total attribution), followed by ET (13–27%) and precipitation (9–22%). Model-based, trend-based, and demographic indicators are combined in a multi-criteria criticality score. Fırat-Dicle, Aras, Büyük Menderes, Antalya, and Susurluk rank highest; Fırat-Dicle is ranked first in 42% of 10,000 Monte Carlo weight perturbations. The result is a relative prioritization of watersheds, not an absolute risk level, intended to support groundwater monitoring and management.

Keywords: Groundwater storage, Critical watersheds, Dominant drivers, Graph WaveNet, SHAP, Türkiye

---

This manuscript is an EarthArXiv preprint and has been submitted for possible publication in a peer-reviewed journal. Please note that this has not been peer-reviewed before and is currently undergoing peer review for the first time. Subsequent versions of this manuscript may have slightly different content.

---

1. Introduction

Groundwater accounts for the largest freshwater resources on Earth and becomes an integral part of the terrestrial water cycle (Aeschbach-Hertig and Gleeson, 2012). Globally, groundwater resources account for around 30% of all freshwaters. Groundwater supplies more than 40% of water demand in irrigated agriculture and hence plays a crucial role in food security (Gleeson et al., 2012; Kuang et al., 2024) and 25% for potable water requirements, and the 10% for industrial applications (Ahmadi et al., 2020). Therefore, groundwater resource quantification is a critical challenge in densely populated regions to provide sufficient amounts of freshwater.

Climate change and the resulting shifts (Yeşilköy and Baydaroğlu, 2025) in the water cycle have accelerated research on groundwater resources (Yeşilköy et al., 2024; Taylor et al., 2013). Various studies have investigated groundwater dynamics across different regions of the world. For instance, Clark et al. (2025) utilized a multilayer perceptron (MLP) neural network model coupled with XAI tools. They aimed to determine whether groundwater level declines in Australia's largest hydrological system were driven by climatic factors or human activities. Their findings revealed that the most critical drivers affecting groundwater level changes were groundwater extraction (number of wells), floods, annual precipitation, and potential evapotranspiration (hereafter "ET"). Chakraborty et al. (2021) investigated the factors influencing groundwater level fluctuations in Texas, USA, utilizing Extreme Gradient Boosting (XGBoost) and XAI. The results indicated that long-term drought indices along with cumulative precipitation deficits, were the most substantial predictors of changes in groundwater levels. Similarly, Li et al. (2024) analyzed groundwater storage dynamics in Shandong Province, China, to examine their driving factors and develop short-term forecasting models. Their findings demonstrated that combining satellite-based data with hydrological models provides highly accurate results for regional groundwater monitoring. Furthermore, they revealed that Support Vector Machine (SVM)-based AI models can be reliably used for short-term water management planning. Adam et al. (2026) combined GRACE satellite data with the Random Forest (RF) method and Global Land Data Assimilation System (GLDAS) surface hydrological models to track groundwater storage dynamics. Raju et al. (2024) tested multiple linear regression and machine learning (ML) algorithms to predict GWS in the Indo-Gangetic Plains of India, using hydroclimatic inputs such as precipitation, ET, soil moisture, and runoff. Among the tested methods, the RF algorithm showed the most stable performance in capturing complex hydroclimatic relationships.

Approximately 18% of Türkiye's total water resource potential comprises groundwater resources. A substantial portion of the flow in major rivers is derived from groundwater via springs and baseflow. The groundwater resources of Türkiye are predominantly situated within alluvial and karst aquifers (Yazicigil and Ekmekci, 2019). Groundwater studies in Türkiye have primarily focused on groundwater characteristics, pollution, including the assessment of arsenic levels (Gunduz et al., 2010), nitrate contamination (Nas and Berktay, 2006; Yesilnacar et al., 2008; Güler et al., 2012), and zinc concentrations (Güler et al., 2012; Kara, 2025) and their associated health impacts (Baba and Tayfur, 2011; Davraz and Batur, 2021). Moreover, several studies have evaluated general groundwater quality indicators (Tayfur et al., 2008; Tokatli et al., 2013;

Kavurmaci and Üstün, 2016; Yetiş et al., 2019; Taşan, 2025) and salinization processes (Güler et al., 2012). Aksoy et al. (2009) investigated the Balçova Geothermal Field in İzmir and reported that the intrusion of toxic elements, such as arsenic, antimony, and boron, into shallow aquifers restricted the use of these waters for household consumption and agricultural irrigation. In a study focusing on Türkiye's 25 watersheds, Dilcan and Koksal (2026) modeled the interactions between water resources, energy production, and climate change for the 2023–2053 period to quantify the freshwater consumption of hydroelectric and fossil-fueled power plants. Furthermore, the Kızılırmak, Euphrates–Tigris, Gediz, Ceyhan, and Sakarya watersheds were identified as areas facing the highest water stress, whereas the Eastern Black Sea, Aras, and Eastern Mediterranean watersheds were classified as more water-secure regions. Several studies have also focused on forecasting groundwater levels and potential at different scales in different part of Türkiye through various methodologies like multiple linear regression (MLR), ANFIS, radial basis neural network (RBNN), and SVM (Demirci et al., 2019), analytical hierarchy process (AHP) and frequency ratio (FR) (Ahmadi et al., 2020), binary logistic regression (Ozdemir, 2011), multi-criteria and heuristic methods (Bozdağ et al., 2025). Ertürk et al. (2014) investigated the impacts of climate change on groundwater resources in the Köyceğiz-Dalyan special environmental protection area within the eastern Mediterranean watershed using the Soil and Water Assessment Tool (SWAT) model. Their simulation results indicated a clear decline in both groundwater recharge and storage. Karatas et al. (2026) evaluated the spatiotemporal variations in groundwater depth (GD) and salinity (e.g., EC) across the southern part of Türkiye. Their findings revealed that the slope of the GD trend increased across nearly the entire area, whereas the slope of the EC trend increased in only 16% of the study region.

This study analyzes the spatiotemporal variations of groundwater storage across Türkiye to identify the most critical watersheds using a multi-criteria approach. The objectives are to identify the watersheds with the most critical GWS conditions and to determine which factor (GWS memory, precipitation or ET) dominates GWS variability in each of them. A prediction model is built as the basis for the attribution.

Our framework consists of five main analytical steps. First, Empirical Orthogonal Functions (EOFs) are applied to GWS, precipitation, and evapotranspiration data for each watershed to achieve dimensionality reduction through principal components. Second, a spatiotemporal prediction model of GWS anomalies (6-month horizon) is constructed using GWN architecture. Third, watershed-specific SHAP values are computed to quantify the impact of individual hydro-climatic variables within the prediction model. Fourth, a watershed criticality score is established for each watershed by fusing historical GWS-derived features with the predictive and explanatory indicators, where relative weights are assigned to each feature. Finally, the sensitivity of the criticality ranking to the assigned weights is examined through One-At-a-Time (OAT) and Monte Carlo (MC) analyses.

2. Materials and Methods

2.1 Study Area

There are twenty-five watersheds (Fig. 1, Latitude: 36-42°N, Longitude: 26-45°E) and important water resource management projects (i.e., the Southeastern Anatolia Project (Güneydoğu Anadolu Projesi (GAP) in Turkish), and hydropower plant facilities across Türkiye. According to the Turkish Statistical Institute (TURKSTAT, 2024; https://veriportali.tuik.gov.tr/en/press/ 53699), the population number is 86.1 million and expected to increase to 94 million by 2050. In addition to population growth, climate change is expected to exacerbate the pressure on water resources due to precipitation instability and increased evaporation from surfaces.

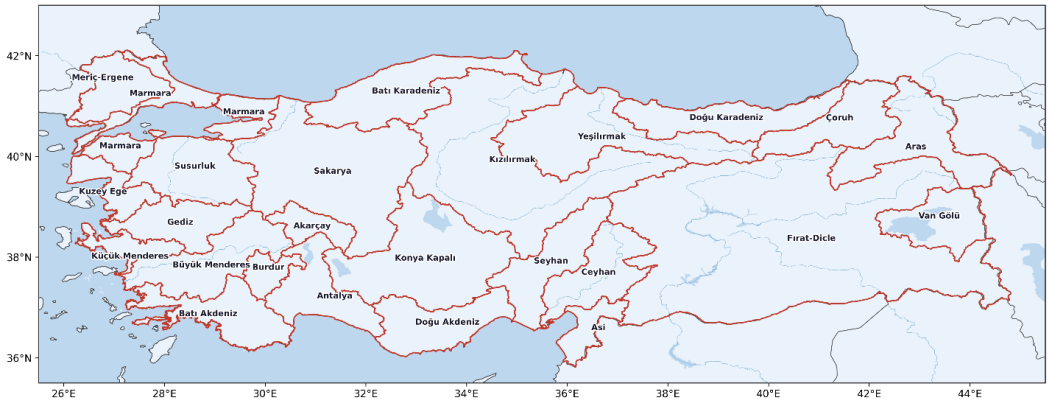


Figure 1. Türkiye's watersheds. Red lines represent the borders of watersheds, and their names are in the center.

2.2 Data

Daily gridded GWS has been downloaded from the National Aeronautics and Space Administration's (NASA) Global Land Data Assimilation System (GLDAS) data (version 2.2) with 0.25° spatial resolution from October 1st, 2003, to September 30th, 2024, through the NASA Goddard Earth Sciences Data and Information Services Center (GES DISC) (Li et al., 2020). GLDAS-2.2 CLSM GRACE-DA1 is a land-surface model product that assimilates GRACE terrestrial water storage observations. Gridded daily ET and hourly precipitation data in the same period have been obtained through the ECMWF's AgERA5 and ERA5-land hourly databases with 0.1° spatial resolution, respectively. Hourly precipitation and daily ET data have been converted to monthly total and daily GWS has been converted to monthly mean because of being a stock variable (Djessou et al., 2022) representing the state of the aquifer at a specific point in time, temporal aggregation has been performed by calculating the arithmetic mean rather than the cumulative sum. This approach ensures physical consistency, as GWS reflects an instantaneous volume, whereas flow variables such as precipitation or evapotranspiration are summed over the respective period. To provide spatial resolution consistency, GWS data have been regridded to 0.1-degree to provide spatial resolution consistency. All data have been partitioned using water years (WY, the total number of WY is 21) from October to September rather than calendar years to preserve seasonal integrity at training/test boundaries. The first 16 water years (October 2003 –

September 2019) are used for model development (training and validation) and the last five water years (October 2019 – September 2024) for testing.

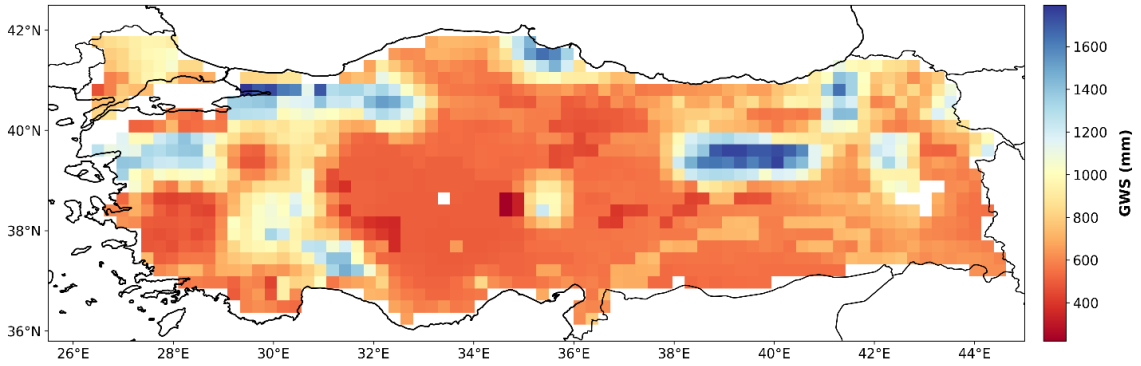


Figure 2. Spatial distribution of GWS in Türkiye between the years 2003 and 2024 (21 water years).

The number of populations at district-level has been obtained through the TURKSTAT and there is a discrepancy between the watershed and the district boundaries. To address this, the areas of the districts located within the watershed boundaries have been calculated, and population figures have been separated according to the area covered by each watershed. This step has been performed with open-access QGIS software (version 3.40) The population density of each watershed can be found in Fig. 3.

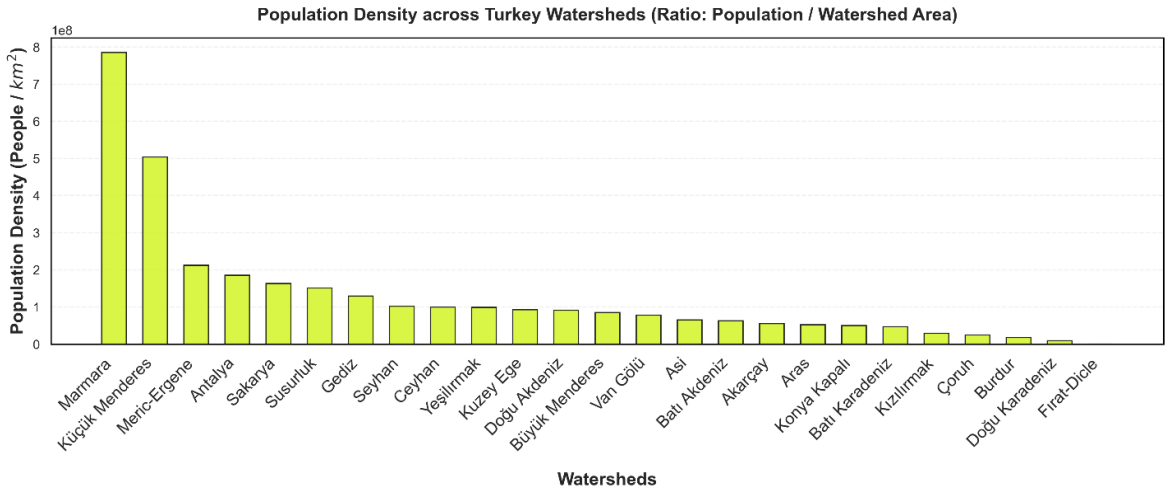


Figure 3. Population density (Population/Watershed Area) across Türkiye watersheds.

2.2.1 Data Normalization

Three distinct normalization procedures have been applied sequentially to ensure methodological consistency and prevent data leakage across training and test periods (Davari et al., 2025). First, EOF input fields have been mean-centered via temporal mean subtraction (anomaly decomposition) following the examples of Conlin et al. (2020) and Fraehr et al. (2022). Subtracting the temporal mean isolates the anomaly field, the departure from the long-term climatological

state, which is the quantity of hydrological interest. Consequently, all EOF principal component scores, and by extension all model predictions, represent GWS anomalies relative to the training-period mean rather than absolute storage values.

Second, the node feature matrix X has been standardized using z-score normalization ($X_{scaled}=\frac{X-\mu_{train}}{\sigma_{train}}$), where μ_{train} and σ_{train} denote the mean and standard deviation computed exclusively over the training period and subsequently applied to both training and test sets. This step is essential because the input features span heterogeneous physical units and magnitude ranges, GWS is expressed in mm, population density in persons/km², and trend slope in mm/month, and without normalization, features with large absolute values would dominate gradient updates during backpropagation, destabilizing training and biasing learned representations toward high-magnitude inputs.

Third, the target variable Y (GWS EOF Mode 1 at forecast horizon $t+h$) has also been z-score normalized using training-period statistics prior to model optimization. Following inference, predictions have been back-transformed to physical units via $\hat{y}_{mm}=\hat{y}_{scaled}\cdot\sigma_{train}+\mu_{train}$. Normalizing the target ensures that the Huber loss function operates on a dimensionless, unit-variance quantity, providing numerically stable gradients regardless of the absolute magnitude of GWS variability across watersheds. The inverse transformation restores interpretable units (mm) for subsequent analysis and visualization.

In all three cases, normalization parameters have been estimated solely from training data and applied to the test set without re-estimation, ensuring strict temporal separation between training and evaluation phases, which prevents test-period information from entering the normalization.

2.3. Methods

The objective of this study is to identify the watersheds of Türkiye with the most critical GWS conditions and to determine which factor dominates GWS variability in each of them. The prediction model is the vehicle for this attribution: SHAP explains what the model uses, so the model has to reproduce the temporal behavior of GWS anomalies. To achieve this, a predictive framework has been developed using EOF (Lorenz, 1956) decomposition and GWN (Wu et al., 2019). Furthermore, XAI has been utilized to analyze the driving factors influencing GWS. A multi-component criticality score has been established to identify the most vulnerable watersheds. To examine the stability of the criticality scores and of the selection of the most critical watersheds, a sensitivity analysis has been conducted using the One-At-a-Time (OAT) (Morris, 1991) and Monte Carlo (MC) (Helton, 1993) simulations.

2.3.1 Empirical Orthogonal Function (EOF)

During the data pre-processing stage, different approaches and testing methods (Baydaroğlu et al., 2024) have been evaluated to identify the most suitable representation of the data for achieving high predictive performance (Baydaroğlu et al., 2025). For the watershed-scale analysis, spatial averaging has not been adopted because the study watersheds differ considerably in size, which

may lead to the loss of important spatial information. Grid-based representation has also been considered; however, treating each grid independently may result in strong redundancy among neighboring grids within the same watershed and may limit the model's ability to learn watershed-scale dynamics.

Therefore, EOF has been employed in the pre-processing stage. EOF provides physically interpretable spatial modes together with corresponding time series for each mode, allowing an efficient representation of the dominant variability patterns while generating suitable inputs for the prediction model.

EOF is a function that enables the decomposition of a continuous space-time field $X(t,s)$, where t and s represent time and spatial position, respectively. $X(t,s)=\sum_{k=1}^{M} c_k(t)u_k(s)$ where M denotes the number of modes present in the field, utilizing an optimal set of spatial basis functions $u_k(s)$ and temporal expansion functions $c_k(t)$ (Hannachi et al., 2007).

EOF analysis has been applied separately to the groundwater storage (GWS), precipitation, and ET data for each watershed. The decomposition has been performed using Singular Value Decomposition (SVD). Figure 4 shows the mode-wise explained variance averaged across all watersheds, together with the corresponding standard deviations (mean ± standard deviation). The dominance of Mode 1 is the most pronounced in ET, followed by GWS and precipitation, with subsequent modes contributing minimally to the total variance.

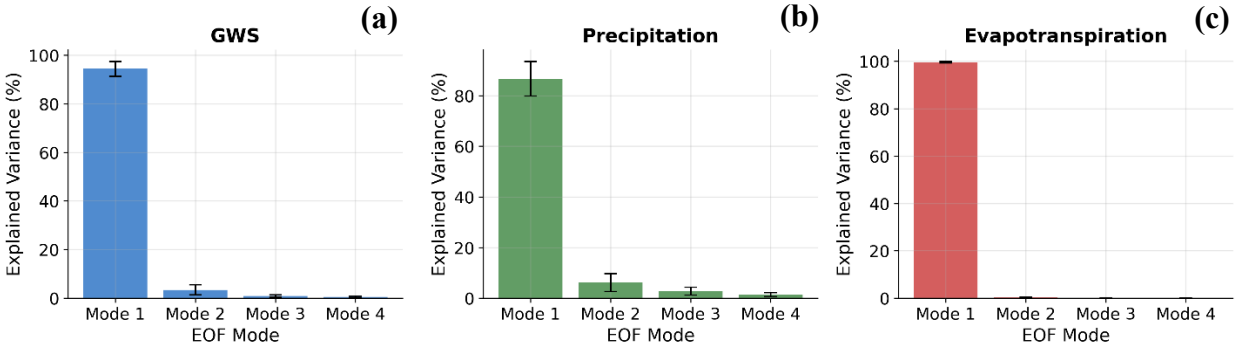


Figure 4. Explained variance by EOF modes for (a) GWS, (b) precipitation, and (c) evapotranspiration. Values indicate the mean ± standard deviation across 25 watersheds.

Following similar approaches in the literature (Wang et al., 2015; Ham et al., 2019), to reduce input dimensionality, the features for the GWS, precipitation, and ET groups have been represented by GWS EOF1–4, Prec EOF1–4, and ET EOF1–4, respectively.

The data pipeline of the model is described below. This process converts high-dimensional pixel-based data into low-dimensional summaries (EOFs). Then, a hybrid deep learning model analyzes both spatial and temporal dependencies.

i) The starting point is high-dimensional raw pixel data ($T \times P_i$), which shows how many pixels (P) in each watershed (i) change over time (T).

ii) EOF analysis has been performed for each watershed using Singular Value Decomposition (SVD). This step produces principal component scores ($T \times K_i$) that

represent the variance of thousands of grids. This reduces the data size, filters out noise, and makes calculations more efficient.

iii) This node feature tensor is used as input for the GWN model. The model simultaneously processes both historical time-series data and the spatial relationships between watersheds.

Additionally, EOF spatial patterns have been estimated exclusively using the training period. To prevent temporal data leakage, test-period PC scores have been obtained by projecting test data onto these pre-computed training EOF patterns. Input features used in the GWN model and GradientSHAP analysis are detailed in Table 1.

Table 1. Input features used in the GWN model and GradientSHAP analysis.

Group	Feature	Type	Description
GWS	EOF Mode 1-4	Dynamic	Principal component scores of GWS anomaly field (monthly mean)
Precipitation	EOF Mode 1-4	Dynamic	Principal component scores of monthly total precipitation
ET	EOF Mode 1-4	Dynamic	Principal component scores of monthly total ET
Watershed Characteristics	GWS mean	Static	Mean GWS anomaly over the last 5 training water years (mm); lower values indicate current water stress
	Standard deviation	Static	GWS variability (mm)
	Minimum GWS	Static	Historical minimum GWS anomaly (mm); proxy for drought vulnerability
	Trend slope	Static	Sen's slope (mm/month; Sen, 1968); trend significance assessed via Mann-Kendall test (Mann, 1945; Kendall, 1975) ($p < 0.05$); long-term depletion rate
	Trend acceleration	Static	Difference between last 5-year slope and long-term slope (mm/month); detects accelerating depletion
	Seasonal amplitude	Static	Peak-to-trough range of Seasonal and Trend decomposition using Loess (STL) (Cleveland et al., 1990; Shamsudduha et al., 2009) seasonal component (mm); recharge seasonality
	Population density	Static	People/km2; proxy for anthropogenic water demand pressure
	Watershed area	Static	km^2; spatial scale of the hydrological unit

Dynamic features vary at each timestep; static features are time-invariant node attributes broadcast across all time steps. EOF modes have been computed separately for each watershed using training-period data only (N=4 modes per variable). All features have been z-score normalized using training-period statistics prior to model input. Static attributes are computed from training-period data (water years 2004–2019) only.

In addition, the GWS EOF1 anomaly is defined as the target variable, representing the millimeter-scale deviation of groundwater storage (GWS) from the training-period mean. The model predicts this anomaly 6 months ahead (h = 6); other horizons are reported in Section 3.2. A 3-month rolling mean has been employed to smooth the GWS time series, thereby mitigating high-frequency noise and enhancing the visibility of underlying trends (Baydaroğlu et al., 2024). Two target forms are compared: the anomaly itself at t+h, and its change relative to the current smoothed

anomaly (the value known at the forecast origin). The form is selected on the validation period only; the change form has been selected (validation RMSE 30.6 mm versus 31.1 mm), and the predicted change is added to the current anomaly to obtain the predicted level.

2.3.2 Graph WaveNet (GWN)

GWS exhibits strong spatiotemporal dependencies: adjacent watersheds may share similar precipitation regimes, recharge dynamics, and in some cases hydraulic connectivity, making the prediction of GWS in one watershed partially dependent on the hydrometeorological state of its neighbors. To exploit these dependencies, this study employs GWN (Wu et al., 2019), a deep learning architecture that combines graph-based spatial convolution with dilated causal temporal convolution within a single framework.

The spatial structure of the problem is encoded as a directed graph $G=(V, E, A)$ where V is the set of nodes, E is the set of edges, and edge weights are defined by a hybrid adjacency matrix: $A=\alpha A_{geo}+(1-\alpha)A_{corr}$, where A_{geo} encodes geographic contiguity (binary indicator of shared watershed boundaries) and A_{corr} encodes pairwise Pearson correlations between GWS EOF Mode1 time series computed during the training period, thresholded at $r>0.3$ to retain only the stronger connections. Equal weighting ($\alpha=0.5$) has been applied to balance physical proximity and hydrological similarity. Both matrices have been row-normalized prior to combination.

A key feature of GWN is the inclusion of a self-adaptive adjacency matrix $\tilde{A}_{adp}$, learned end-to-end during training: $\tilde{A}_{adp}=softmax(ReLU(E_1 E_2^T))$, where $E_1, E_2 \in R^{N\times d}$ are trainable node embedding matrices. This component allows the model to capture latent spatial dependencies not encoded in the predefined adjacency structure. The final adjacency used in each graph convolution layer is $A_{final}=0.5\ A+\ 0.5\ \tilde{A}_{adp}$

Figure 5 shows graph Adjacency matrix based on geographic contiguity and GWS correlation.

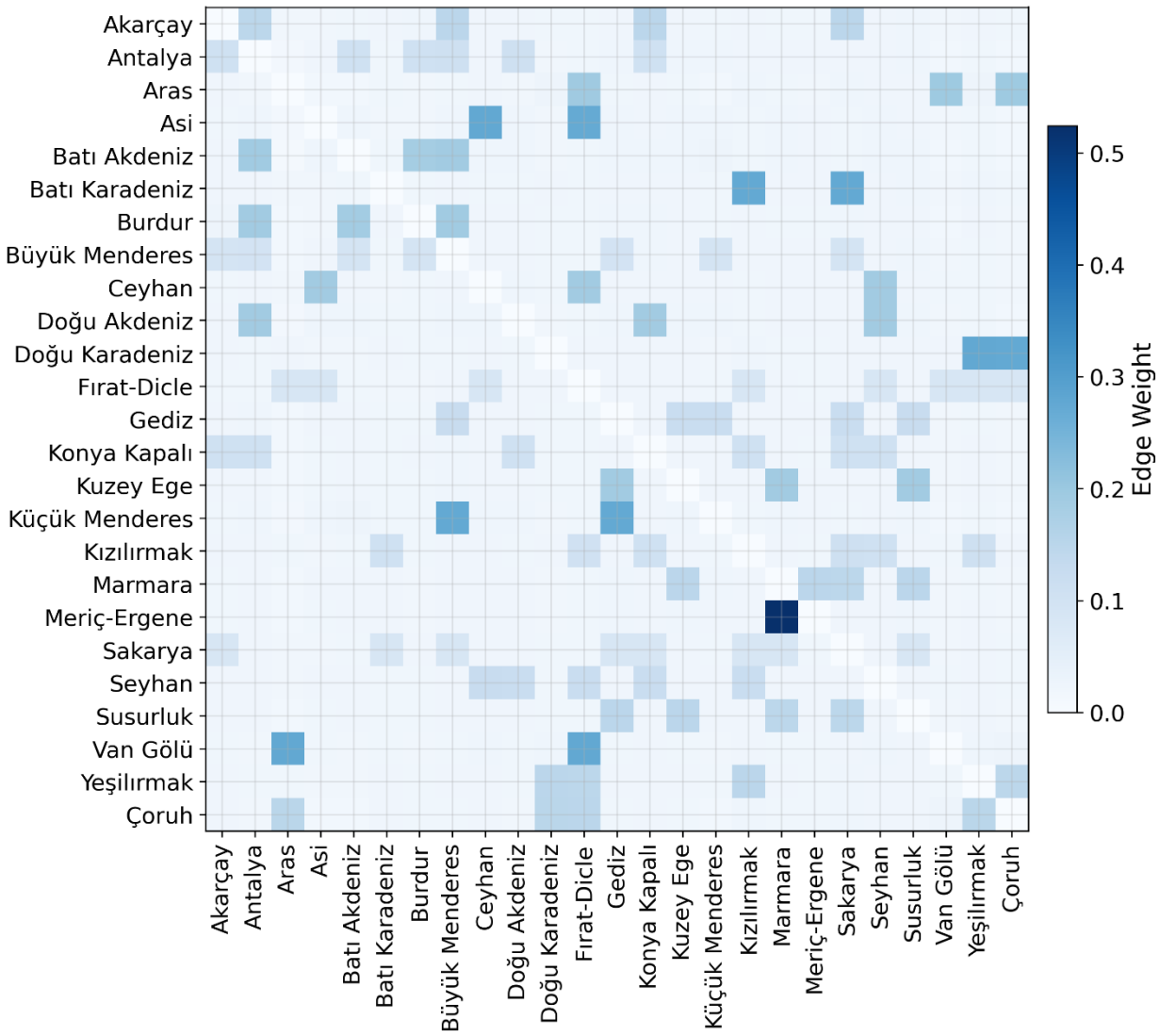


Figure 5. Graph Adjacency matrix based on geographic contiguity and GWS correlation.

Temporal dependencies are captured through stacked dilated causal convolution layers with exponentially increasing dilation factors d=1,2,4,8. The progressively increasing dilation factors allow the model to capture temporal dependencies over multiple time scales by expanding the receptive field in successive layers. In this framework, the first layer primarily captures short-term variations (1–3 months), while subsequent layers extract medium-term (2–6 months), seasonal (4–12 months), and longer-term (up to 16 months, the receptive field of the stack) temporal patterns. This multi-scale design, adopted from the WaveNet architecture, enables efficient modeling of both local and long-range temporal dynamics without a substantial increase in computational complexity. Gated activations of the form: $z=tanh(W_f * x) \odot \sigma(W_g * x)$, where * denotes convolution, $\odot$ denotes element-wise multiplication, regulating information flow through the network analogously to the gating mechanism in LSTM architectures, but with greater

computational efficiency and explicit multi-scale temporal receptive fields. Here, x denotes the input hidden-state tensor from the previous layer, W_f and W_g are the convolutional weights of the filter and gate branches, respectively, $tanh(\cdot)$ is the filter activation function, $\sigma(\cdot)$ sigmoid gate activation function, and z (output) is the resulting gated output passed to the subsequent layer.

The model receives as input the node feature tensor $X \in R^{T_{seq} \times N \times F}$, where T_{seq}=24 months (input window), N=25 watersheds, and F=20 features per node (12 dynamic EOF modes + 8 static watershed characteristics), and produces a single forecast $\hat{y}_{t+h} \in R^N$ for horizon $h \in \{1, 3, 6, 12, 24, 36\}$ months. Model parameters have been optimized using the Adam optimizer (Kingma and Ba, 2015; Baydaroğlu and Demir, 2024) (learning rate 3×10^{-4}, weight decay 5×10^{-4}) with a Huber loss function (δ=1.0) and cosine annealing warm restart scheduling (Loshchilov and Hutter, 2017). The data are split chronologically according to the month being predicted (forecast month = forecast origin + 6 months). Input–output pairs whose predicted month falls up to September 2017 form the training set, those with a predicted month in October 2017 – September 2019 the validation set (early stopping and model selection), and those with a predicted month in October 2019 – September 2024 the independent test set. EOF patterns, normalization statistics, static attributes and the correlation part of the adjacency matrix are estimated from the first 16 water years (October 2003 – September 2019) only. No test-period value enters training or validation, and the test set is used neither for early stopping nor for the selection of the target form. The 24-month input windows of the first test pairs extend into the validation period, as in any forecasting setting, but they contain no information on the months being predicted.

The GWN model predicts the normalized EOF1 anomaly of GWS for a given prediction horizon. The predicted EOF1 values are then converted back to GWS anomalies using inverse scaling. Specifically, the model output (standardized EOF Mode 1 score) is first inverse z-score transformed using the training-period mean and standard deviation of the predicted month, yielding predicted GWS anomalies in the original physical units (mm). When the change form is selected, the predicted change is added to the current smoothed anomaly to obtain the predicted level.

This integrated framework is designed to capture both temporal dynamics and spatial dependencies in groundwater systems while reducing the dimension of the original gridded dataset. Consequently, the dominant spatiotemporal variability is retained in a compact input representation. The hyperparameters adopted for the GWN model are listed in Table 2.

Table 2. Hyperparameters used in the GWN model

Parameter	Value	Explanation
N_EOF	4	Number of EOF modes per variable
SEQ_LEN	24 months	Input sequence length (receptive field = 16 months)
FORECAST_HORIZON	6 months	Forecast horizon (main experiment; 1, 3, 12, 24 and 36 months in Table 6)
GWN_HIDDEN	32	Hidden layer dimensionality
GWN_LAYERS	4	Number of WaveNet layers (dilation=1,2,4,8)

GWN_DROPOUT	0.4	Dropout rate for regularization
BATCH_SIZE	8	Mini-batch size
N_EPOCHS	150	Maximum training epochs
Learning rate	$3x10^{-4}$	Adam optimizer initial learning rate
Weight decay	$5x10^{-4}$	L2 regularization coefficient
PATIENCE	30	Early stopping patience
VAL_MONTHS	24	Validation predicted months (October 2017 – September 2019), used for early stopping and model selection
Correlation threshold	0.3	Minimum Pearson r for adjacency matrix edge inclusion
Huber loss	1.0	Transition point between L2 and L1 loss regions
Scheduler	CosineAnnealingWarmRestarts	T_0=30, T_{mult}=2, η_{min}=10^{-5}
Optimizer	Adam	β_1=0.9, β_2=0.999 (PyTorch defaults)

All hyperparameters have been set prior to training with reference to the original GWN implementation (Wu et al., 2019) and held constant across all watersheds and all forecast horizons (h = 1, 3, 6, 12, 24, 36 months). Early stopping and model selection use the validation period only.

2.3.3 Explainability and Criticality

Traditional approaches that rely exclusively on groundwater trends may categorize watersheds with analogous diminishing storage patterns into the same risk classification. The suggested SHAP-based Criticality Score system characterizes the model-based drivers and the vulnerability of each watershed. A watershed exhibiting a continual decrease in GWS and a feeble seasonal recharge signal may be intrinsically more susceptible than a watershed with a similar dropping trend but a robust seasonal cycle. The methodology integrates predictive, explanatory, and historical groundwater indicators to identify watersheds with diminished recovery potential and increased criticality, thus facilitating better informed groundwater management decisions.

Following the feature engineering and XAI paradigm commonly used in the literature, feature attribution has been performed using GradientSHAP (Captum library; Kokhlikyan et al., 2020), an implementation of the SHAP framework adapted for gradient-based deep learning models for SHAP analysis and watershed criticality assessment. These features included the long-term GWS trend (Mann–Kendall), GWS trend acceleration (GWS 5-year trend minus long-term trend), mean GWS (last five training water years), GWS variability (standard deviation), minimum GWS, GWS seasonal amplitude, and population densities of watersheds. These features have been subsequently integrated into the criticality assessment framework to provide a comprehensive evaluation of watershed conditions and resilience.

The workflow of this research stage proceeds as follows: First, to understand the driving factors behind the predictions, SHAP values have been determined individually for each watershed using the GWS anomaly prediction model. This watershed-specific approach has been adopted because each watershed exhibits distinct environmental and hydrogeological characteristics, allowing the model to quantify the exact contribution and influence of each input variable per

watershed. Subsequently, a criticality score has been established for each watershed by utilizing the derived features, the model predictions, and the calculated SHAP values as independent features, where a specific weight is assigned to each feature component. To examine how sensitive the computed criticality scores are to the assigned weights, a sensitivity analysis is conducted. This analysis employs the widely-used OAT (Saltelli et al., 2008; Owais and Ramadan, 2025) alongside the MC methods (Helton, 1993; Ge and Asgarpoor, 2011). This dual assessment shows how stable the final watershed ranking is with respect to the weight selection.

2.3.3.1 Explainability

Unlike traditional AI methods that operate as black-box systems, XAI approaches, such as SHAP analysis, have been developed to improve transparency and interpretability by quantifying the contribution of specific variables to model predictions (Demiray et al., 2025). SHAP is a widely utilized XAI method grounded in cooperative game theory (Shapley, 1953). It aims to explain predictive models by treating every feature (or predictor) as a player and the model outcome as the payout (Lundberg and Lee, 2017; Salih et al., 2025). A primary strength of SHAP is its capacity to quantify both the magnitude and direction of a feature's influence on a specific prediction, thereby facilitating both global and local interpretability (Lundberg et al., 2020; Mermer et al., 2026).

SHAP analysis is applied to dynamic inputs (GWS, precipitation and ET EOF modes). The watershed characteristics (Table 1) are also model inputs, but they are constant in time for each watershed, so GradientSHAP attributes zero importance to them by construction; they enter the criticality score directly instead. Variability and seasonal amplitude are included in the score to characterize the short-term and long-term vulnerability of the watersheds. In addition to the GWS trend, GWS trend acceleration has been included as a complementary feature. This inclusion is critical for distinguishing between watersheds that exhibit identical trend magnitudes but different temporal dynamics. For instance, two watersheds may both show a long-term trend of -3 mm/year; however, one might be decelerating to -1 mm/year over the last five years, while the other is accelerating to -8 mm/year. While their average trends appear identical, their levels of criticality differ significantly. Incorporating acceleration allows the score to capture this distinction. SHAP attributions describe how the trained model uses its inputs; they are not causal effects of the physical variables.

2.3.3.2 Criticality

Despite Türkiye’s rich groundwater potential, climate variability and human water use make a detailed assessment of GWS depletion necessary. This phase of the study focuses on identifying watersheds in a critical condition through a multi-dimensional criticality score. Table 3 presents the specific features and weighting factors used to determine this score.

Table 3. Features and their corresponding weights utilized in calculating the criticality score.

Feature	Weights (%)
Prediction	20
SHAP	15
GWS trend	15
GWS trend acceleration	10
GWS mean	10
GWS variability	10
GWS minimum	5
GWS Seasonal amplitude	5
Population density	10

The sensitivity of the ranking to these weights is evaluated through OAT and MC sensitivity analyses presented in Section 2.3.4. Each component is oriented so that higher values indicate higher criticality (lower predicted anomaly, steeper and accelerating decline, lower GWS mean and minimum, larger variability, seasonal amplitude and SHAP pressure, higher population density), min–max scaled to [0,1] and combined with the weights above. The final score is min–max scaled again, so it expresses relative criticality among the 25 watersheds, not an absolute risk level.

In the determination of the criticality score, both the model predictions and their corresponding SHAP values have been treated as distinct features. The prediction represents the model's estimate of GWS conditions with a 6-month lead time (mean predicted anomaly over the test period). In essence, it serves as a synthesis of all learned information, including temporal patterns, cross-watershed relationships, and feature interactions, indicating the expected storage anomaly. SHAP values, on the other hand, measure the contribution and significance of each feature to the model's output. The total absolute SHAP value of the dynamic drivers ("SHAP pressure") is used as a measure of how strongly the predicted GWS of a watershed responds to its hydro-climatic inputs. It is a sensitivity measure, not a measure of predictive uncertainty or reliability: watersheds whose predictions respond more strongly to the drivers receive a higher score.

The composite index is min–max scaled to [0,1] and therefore expresses criticality relative to the other 25 watersheds. For interpretation, three classes are used: low (< 0.20), medium (0.20–0.50) and high (≥ 0.50) relative criticality, where the high class contains watersheds whose score lies in the upper half of the index range. Figure 6 shows the flowchart of the integrated GWS prediction, explainability and criticality scoring framework.

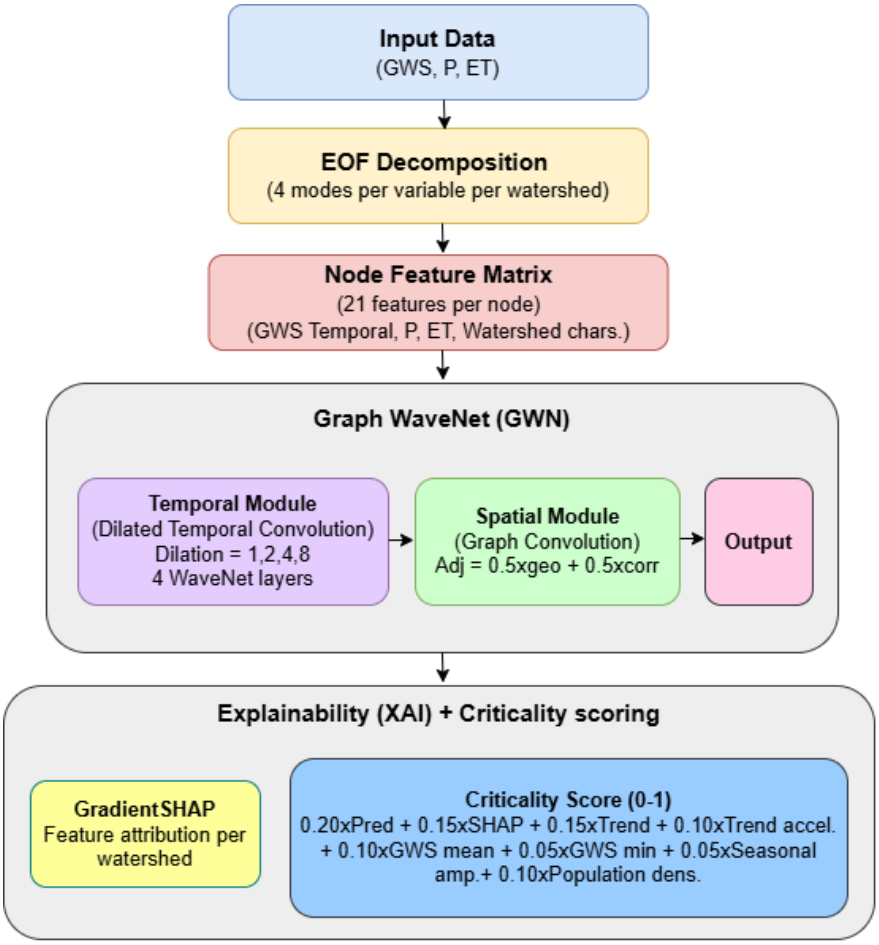


Figure 6. Flowchart of the integrated GWS prediction, explainability, and criticality scoring framework.

2.3.4 Sensitivity Analysis

While the integration of SHAP values and model predictions provides a framework for identifying critical watersheds, the resulting criticality scores depend on the assigned feature weights, and their sensitivity to these weights therefore needs to be examined. To evaluate the stability of these rankings and assess the impact of weight uncertainty, a two-stage sensitivity analysis has been conducted using OAT and MC simulations. The primary objective of this analysis is to examine the stability of the established prioritization; specifically, it addresses whether the identified critical watersheds remain consistent under varying weighting scenarios. By quantifying the stability of the ranking, we examine whether the identified priorities depend on the particular weights chosen.

2.3.4.1 One-at-a-time (OAT)

In OAT sensitivity analysis, each factor is varied separately around a base case (Di Lullo et al., 2020). In this study, OAT analysis varied each component weight from 0% to 200% of its baseline

value while rescaling the remaining weights proportionally, measuring the mean absolute rank change across all watersheds.

2.3.4.2 Monte Carlo (MC)

MC simulation is a statistical approach that uses repeated random sampling of input variables to produce several random simulations of a defined scenario (Castillo et al., 2022). For the sensitivity analysis, an MC simulation (n=10000 iterations) sampled weight vectors from a Dirichlet distribution with concentration parameters proportional to the baseline weights ($\alpha = w_{baseline} \times 10$), yielding perturbed but realistic weight combinations. For each iteration, the full criticality score has been recomputed, and watershed ranks have been recorded. Rank stability has been quantified as the probability of each watershed being ranked first and by the 5th–95th percentile range of its rank.

The methodology has been implemented in Python, leveraging PyTorch for GWN construction, Captum for GradientSHAP attribution, scipy.linalg.svd for EOF analysis, and pymannkendall for Mann-Kendall trend testing.

2.3.5 Performance Criteria

This study uses four metrics to evaluate the prediction model on the test period: the Nash–Sutcliffe efficiency (NSE) $NSE=1-\frac{\sum_{i=1}^{n}(X_i-Y_i)^2}{\sum_{i=1}^{n}(X_i-\overline{X})^2}$, the Pearson correlation coefficient (r) $r=\frac{\sum_{i=1}^{n}(X_i-\overline{X})(Y_i-\overline{Y})}{\sqrt{\sum_{i=1}^{n}(X_i-\overline{X})^2\sum_{i=1}^{n}(Y_i-\overline{Y})^2}}$, the mean bias $Bias=\frac{1}{n}\sum_{i=1}^{n}(Y_i-X_i)$ and the root mean square error (RMSE) $RMSE=\sqrt{\frac{1}{n}\sum_{i=1}^{n}(Y_i-X_i)^2}$, where X and Y denote the observations and the predictions, $\bar{X}$ and $\bar{Y}$ their means, and n the number of values. Bias is the mean of prediction minus observation (mm); positive values indicate overestimation. Percentage-error metrics like MAPE have not been used: GWS anomalies are centered on zero, so MAPE is unbounded when an observation approaches zero. Metrics are computed for each watershed on the test period; pooled values use all watershed–month pairs.

3. Results and Discussion

3.1. GWS Spatial Analysis

Türkiye GWS hotspot analysis can be seen in Figure 7. It shows the spatial distribution of GWS trends throughout Türkiye from 2003 to 2024. Negative GWS trends (red shades), indicating a decline in GWS, are predominantly observed in the eastern, southeastern, and western parts of the study area. In contrast, positive trends (blue shades), representing increasing GWS, are mainly concentrated in the central and western Black Sea Region (“Batı Karadeniz” in Turkish), with smaller localized areas also exhibiting increasing trends.

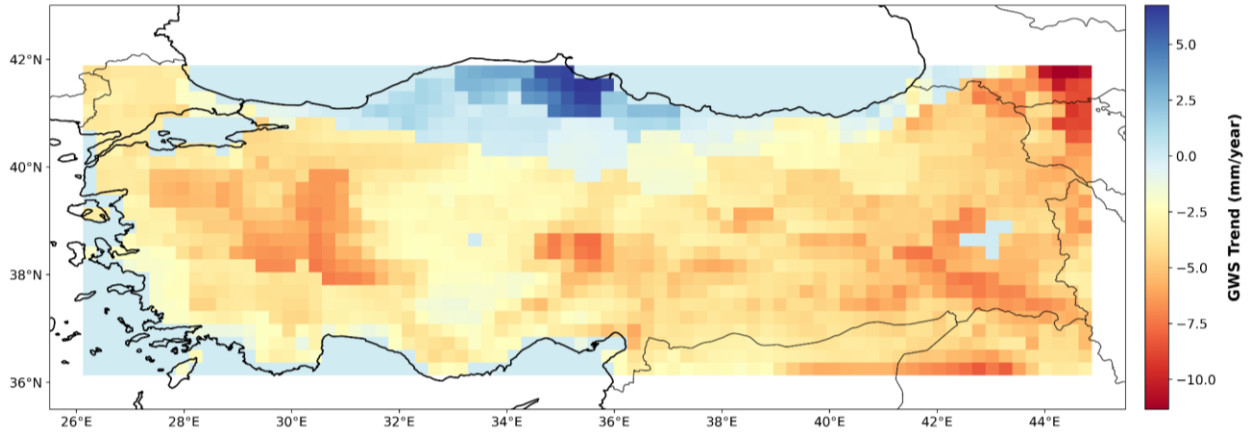


Figure 7. Spatial distribution of GWS trends (hotspot analysis) in Türkiye between the years 2003 and 2024.

3.1.1 Spatial analysis based on 10-year periods' seasons

Figure 8 compares the seasonal average spatial distribution of GWS between Period I (2004–2014 WYs) and Period II (2015–2024 WYs). Overall, the spatial distribution of GWS remains broadly consistent across the two periods. Nevertheless, Period II exhibits a noticeable expansion of low-GWS areas (red shades) in several regions, particularly across the central, the southeastern, and the western parts of Türkiye. In contrast, relatively high GWS values (blue shades) remain concentrated mainly along the northern coast of Türkiye. Seasonal differences are evident (Fig. 8), with summer and autumn displaying the most extensive low-GWS conditions, whereas winter and spring show relatively higher GWS due to seasonal recharge. These results suggest that although the overall spatial pattern is preserved, groundwater availability has generally declined during the more recent decade.

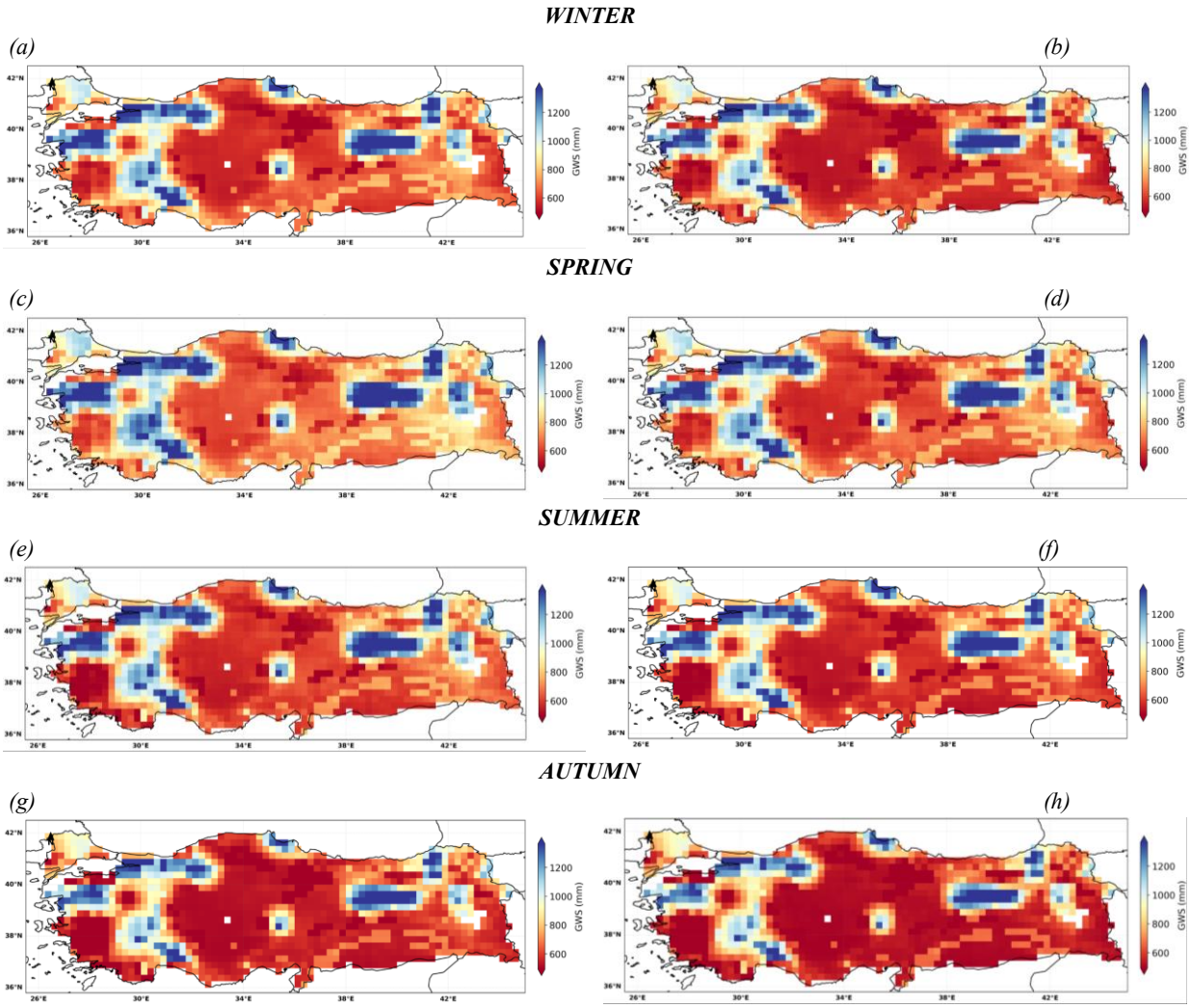


Figure 8. Mean spatial distribution of GWS in winter of (a) Period I, (b) Period II; in spring of (c) Period I, (d) Period II; in summer of (e) Period I, (f) Period II; in autumn of (g) Period I, (h) Period II.

3.1.2 Spatial detrended analysis based on 10-year periods' seasons

Figure 9 presents the seasonal average detrended GWS for Period I and Period II. Following the removal of the long-term trend, the remaining patterns primarily reflect seasonal groundwater variability. Overall, the spatial distribution of detrended GWS remains consistent between the two periods, indicating that the seasonal recharge–discharge cycle is largely preserved across Türkiye. Positive GWSs are predominantly observed during winter and spring, reflecting enhanced groundwater recharge associated with increased precipitation and snowmelt, and reduced ET. In contrast, summer and particularly autumn are characterized by widespread negative GWSs, consistent with seasonal groundwater depletion associated with increased ET and water use. Compared with Period I, Period II exhibits slightly more extensive and pronounced negative GWS values during the dry seasons, suggesting an intensification of seasonal groundwater deficits despite the removal of the long-term trend.

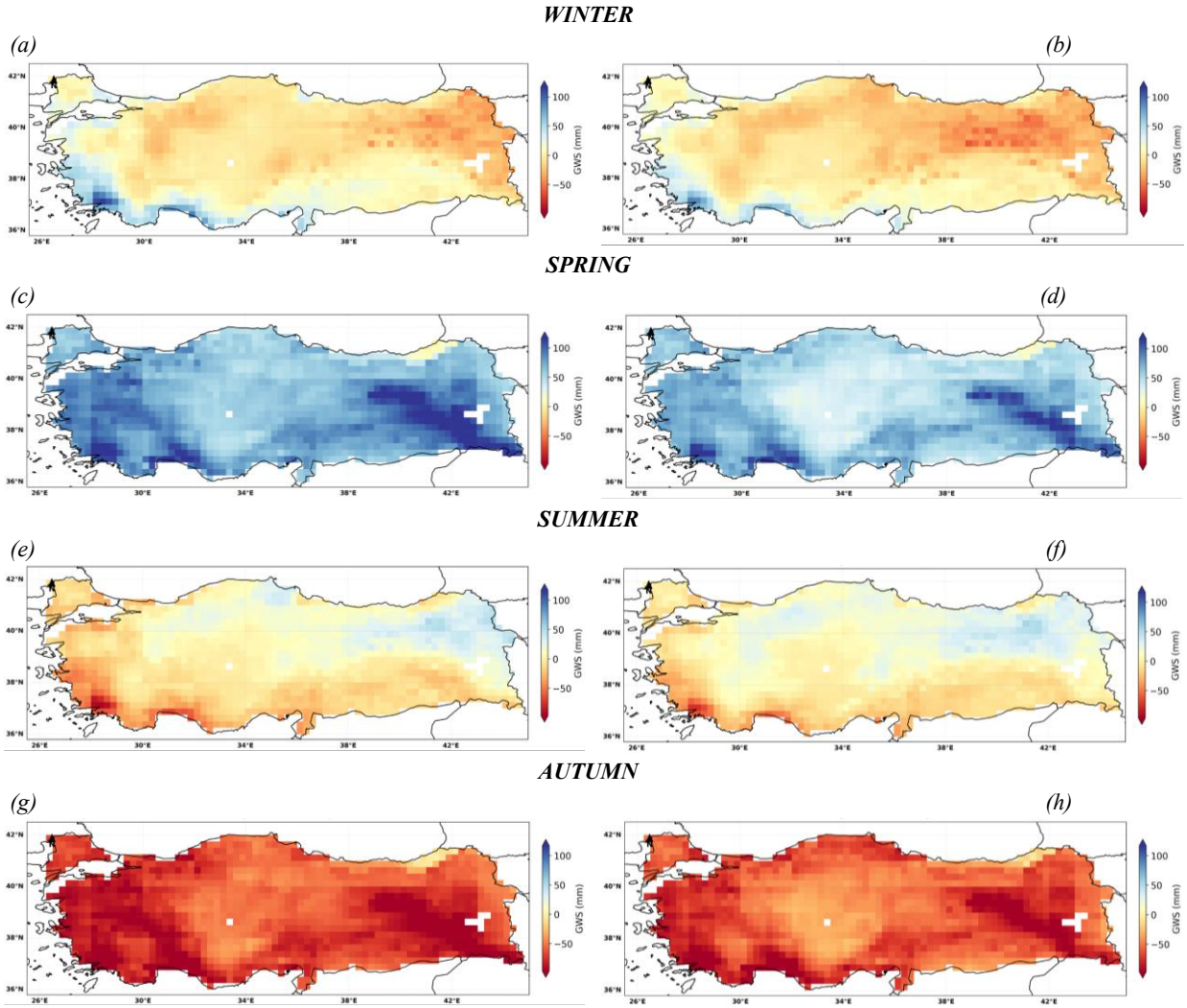


Figure 9. Mean spatial detrended distribution of GWS in winter of (a) Period I, (b) Period II; in spring of (c) Period I, (d) Period II; in summer of (e) Period I, (f) Period II; in autumn of (g) Period I, (h) Period II.

3.1.3 Spatial anomaly analysis based on 10-year periods' seasons

Figure 10 compares the seasonal GWS anomaly distributions between Period I and Period II. A clear shift in anomaly patterns is observed across all seasons. During Period I, positive GWS anomalies dominate much of Türkiye, indicating GWS conditions above the long-term seasonal average. In contrast, Period II is characterized by predominantly negative anomalies, particularly across the central, the eastern, and the southeastern parts of Türkiye, suggesting GWS below the seasonal climatology. Although localized positive anomalies remain in parts of the northern and northeastern regions, the widespread transition from positive to negative anomalies indicates a substantial deterioration in groundwater conditions during the more recent decade. This shift is evident throughout the year and is particularly pronounced during winter and spring, implying that

reduced GWS is no longer limited to the dry season but has become a persistent feature across multiple seasons.

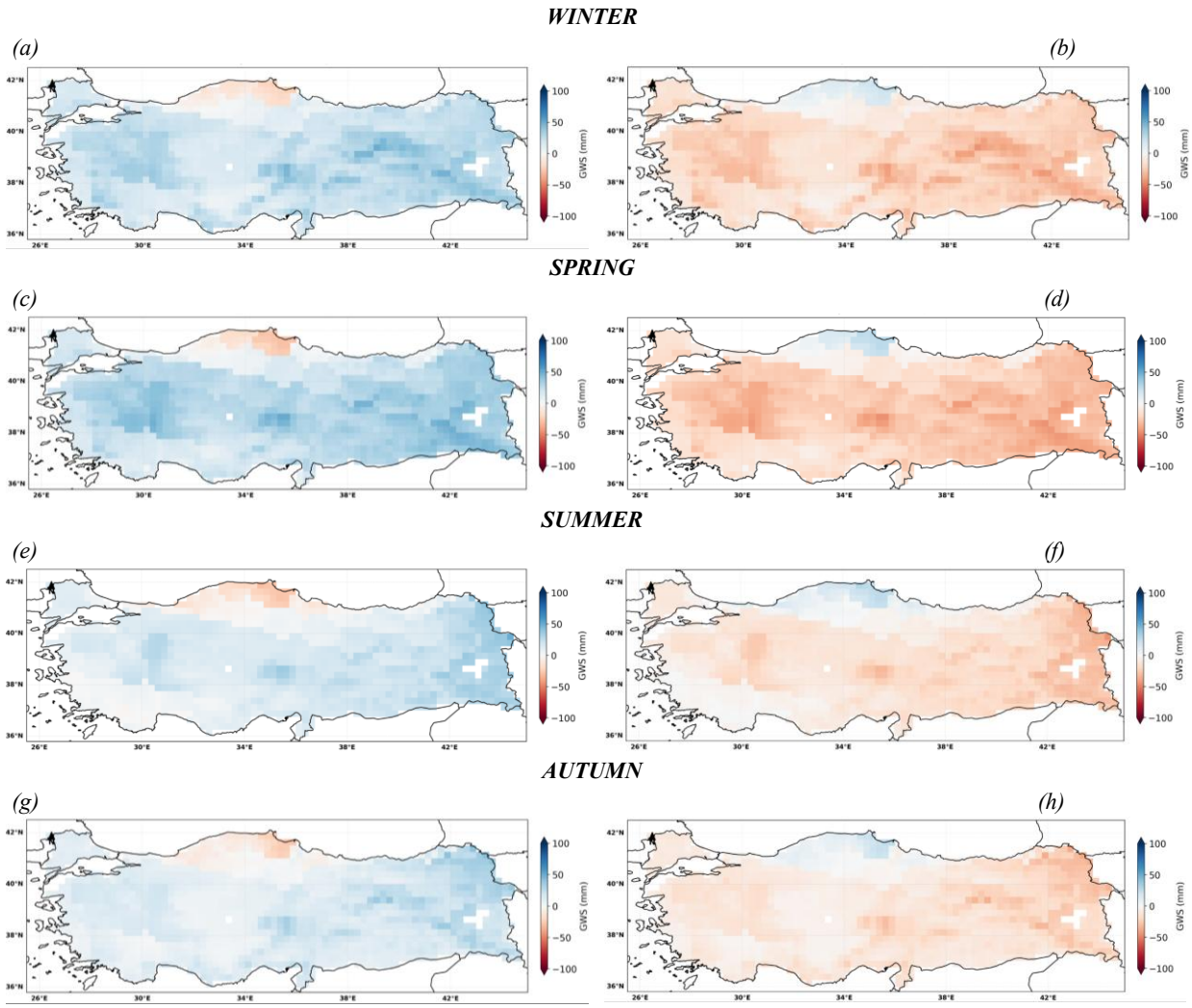


Figure 10. Spatial anomaly distribution of GWS in winter of (a) Period I, (b) Period II; in spring of (c) Period I, (d) Period II; in summer of (e) Period I, (f) Period II; in autumn of (g) Period I, (h) Period II.

3.1.4 Spatial mean analysis based on 21 water years for each watershed

Figure 11 presents the watershed-averaged GWS time series for the 25 main watersheds in Türkiye with their corresponding linear trends. Considerable spatial heterogeneity is evident among the watersheds in both the magnitude and temporal variability of GWS. Most watersheds exhibit negative long-term trends, although the rate of GWS decline varies substantially from one watershed to another. In contrast, only one watershed, the Western Black Sea, displays a slightly increasing trend.

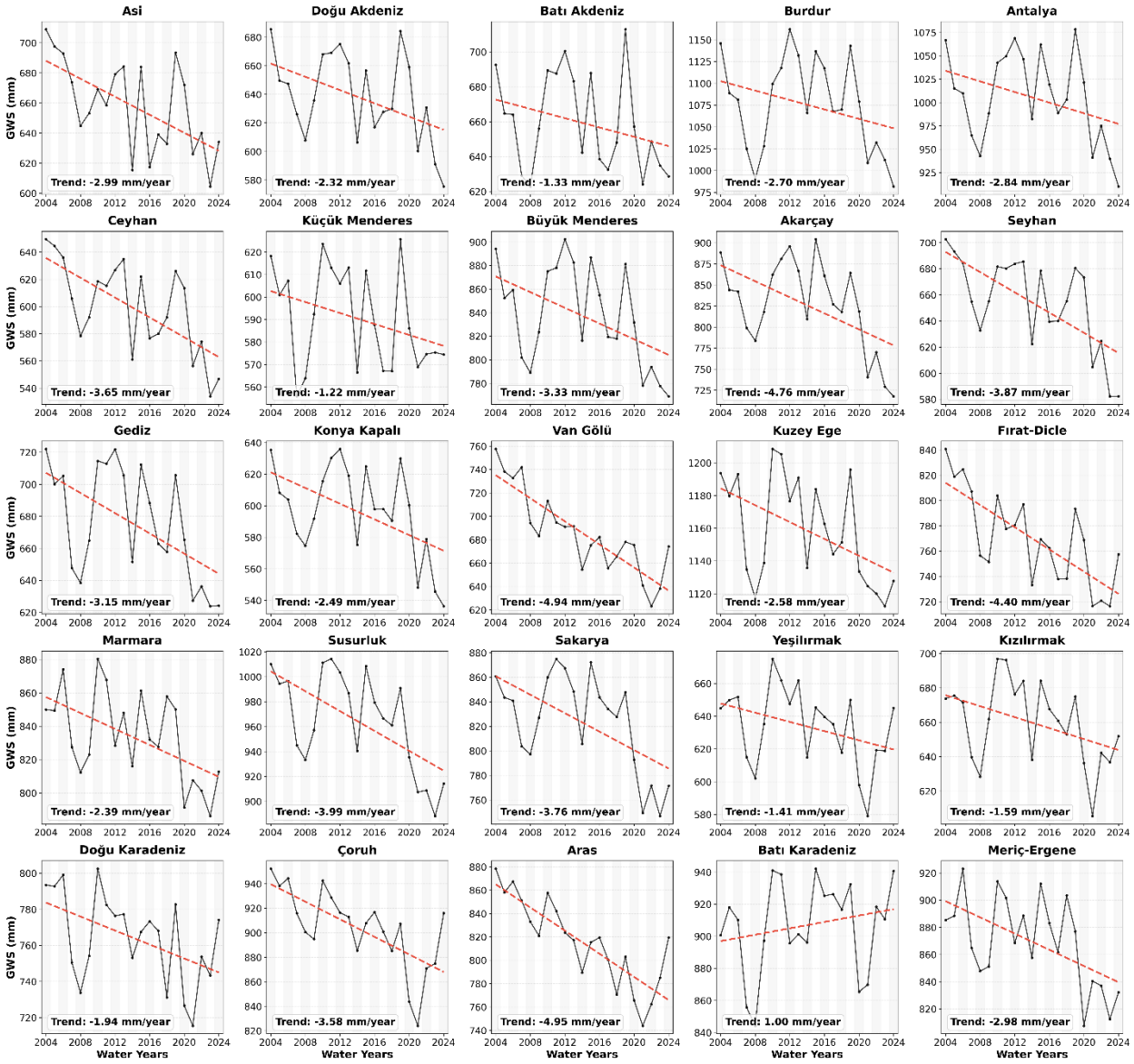


Figure 11. Mean GWS time series and long-term trends for the 25 watersheds.

3.2. Predictive Model

A predictive model based on the GWN architecture has been constructed to model GWS anomalies across Türkiye's watersheds. Figure 12 displays the scatter plot of the observed versus predicted GWS anomalies across the independent test period, aggregating the results of all 25 individual watersheds into a unified visualization (comprising a total of 1500 data).

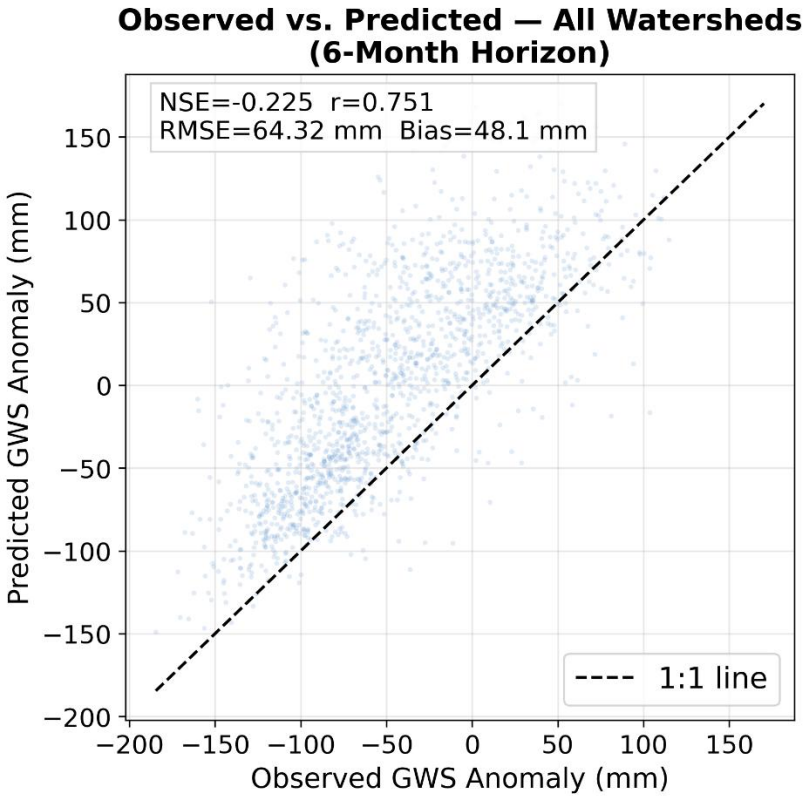


Figure 12. Observed versus predicted GWS anomaly values at the 6-month horizon aggregated across all 25 watersheds and the entire test period (October 2019 – September 2024), yielding NSE = −0.225, r = 0.751, RMSE = 64.32 mm and bias = +48.1 mm. Each point represents a monthly prediction for one watershed. The dashed line indicates the 1:1 reference line.

The predictive performance of the GWN model has been evaluated by multiple metrics, including NSE, r, bias and RMSE (Section 2.3.5). Table 4 presents the overall performance metrics of the 6-month prediction model on the test period, evaluated individually for each watershed.

Table 4. Performance evaluation metrics of the 6-month GWS anomaly prediction across each individual watershed using GWN (test period, October 2019 – September 2024).

Watershed	NSE	r	Bias (mm)	RMSE (mm)
Akarçay	-0.837	0.657	58.3334	74.701
Antalya	-0.273	0.805	68.847	84.609
Aras	0.371	0.878	34.0019	43.280
Asi	0.305	0.798	28.4484	46.059
Batı Akdeniz	-0.118	0.877	59.8245	71.554
Batı Karadeniz	0.214	0.590	18.1251	57.197
Burdur	-1.594	0.682	74.4429	87.701
Büyük Menderes	-0.727	0.764	59.5839	75.117
Ceyhan	-0.171	0.739	45.5051	61.135

Doğu Akdeniz	0.089	0.799	43.376	57.320
Doğu Karadeniz	0.009	0.628	25.0515	47.097
Fırat-Dicle*	-0.083	0.728	40.5779	58.962
Gediz	-0.739	0.784	60.1964	74.014
Konya Kapalı	-0.614	0.691	37.0409	48.100
Kuzey Ege	-0.187	0.796	49.0856	60.259
Küçük Menderes	-0.447	0.857	60.6158	73.689
Kızılırmak	-0.267	0.809	36.0986	46.497
Marmara	-0.349	0.829	50.9537	60.924
Meriç-Ergene	-1.114	0.779	53.6139	65.827
Sakarya	-1.542	0.599	53.9517	66.401
Seyhan	-0.466	0.699	51.8463	68.757
Susurluk	-0.977	0.704	61.6869	80.929
Van Gölü	-0.511	0.798	49.9518	60.643
Yeşilırmak	0.204	0.798	32.3415	45.046
Çoruh	-0.219	0.805	50.0912	61.663
Pooled (all watersheds)	-0.225	0.751	48.1437	64.322

*Fırat-Dicle is “Tigris-Euphrates” in English.

Table 5. Comparison of the GWN model with persistence and linear-trend benchmarks at the 6-month horizon (mean of the per-watershed NSE on the test period).

	NSE (mean)	r	Bias (mm)	Number of NSE+ watersheds
GWN (6 months)	-0.40	0.75	+48	6/25
Persistence	-2.49	-	-	-
Linear trend	-0.89	-	-	-

Table 6. Test-period performance of the GWN model at different forecast horizons (each horizon is a separately trained model). NSE: mean over the 25 watersheds; r, bias and RMSE: median over the 25 watersheds; NSE > 0: number of watersheds with positive NSE.

Horizon (months)	**Mean NSE**	**NSE > 0**	**Median r**	**Median bias (mm)**	**Median RMSE (mm)**
1	0.99	25/25	0.995	+2.1	5.6
3	0.66	25/25	0.892	+18.2	30.7
6	−0.40	6/25	0.784	+50.1	61.1
12	0.18	19/25	0.733	+14.8	45.0
24	−0.78	8/25	0.783	+51.4	64.1
36	−0.47	11/25	0.684	+41.2	59.5

At the 6-month horizon the model reproduces the temporal pattern of the observed anomalies (pooled r = 0.75; r between 0.59 and 0.88 across watersheds, median 0.78) but not their level. The pooled NSE is −0.23 and is positive in only 6 of the 25 watersheds, and the bias is positive in all 25 watersheds (18–74 mm; pooled +48 mm) (Table 4). The bias is a nearly constant offset (Figure 12): the observed anomalies of the test period are on average about 46 mm below the training-period mean, whereas the predictions remain close to zero, i.e., the model has learned the training-period level and does not follow the persistent decline of the last five water years. NSE penalizes such an offset strongly, whereas r does not, so NSE is low although r is high. NSE < 0 means that the predicted levels are less accurate than the test-period mean of the observations, which is a demanding reference because it is not known at the forecast time.

The GWN model performs better than both simple benchmarks (Table 5). Persistence (the anomaly at the forecast origin carried forward) has a mean NSE of −2.49, because the anomalies follow a strong annual cycle and a six-month lag falls in the opposite season; a linear-trend extrapolation gives −0.89. The GWN model outperforms persistence in all 25 watersheds and the trend extrapolation in 19 of them.

Skill depends strongly on the horizon (Table 6). One-month and three-month predictions are accurate (mean NSE 0.99 and 0.66, positive in all 25 watersheds), which largely reflects the persistence of the smoothed series. At 6–36 months the NSE is low or negative and the median bias is positive (+15 to +51 mm), while the median r remains between 0.68 and 0.78. The 12-month model performs better than the 6-month model (mean NSE 0.18; positive in 19 of 25 watersheds); because each horizon is a separately trained model, we do not interpret this non-monotonic pattern physically. The 6-month horizon was adopted for the driver analysis after exploratory runs at the originally planned 5-year horizon (and at 3 years) gave pooled NSE values below zero.

The model is therefore not intended for forecasting GWS levels; it serves as the basis for the attribution analysis. Its role here is to provide a function of GWS history, precipitation and ET whose sensitivities can be examined with SHAP. Because the model captures the temporal dynamics but not the shift in level, the attributions in Section 3.3 describe how the model uses its inputs to reproduce the dynamics of the anomalies; they are model-based indications of driver importance, not causal effects, and the criticality ranking in Section 3.4 is a relative prioritization. The alternative target form (anomaly level instead of change) was not selected on the validation period and gave a pooled test NSE of −0.34.

3.3. Driver attribution with SHAP analysis

In this study, GradientSHAP has been employed to analyze the contribution of GWS history, precipitation and ET to the predicted GWS anomaly using the GWN model. Watershed characteristics are not attributed because they are constant in time (Section 2.3.3.1).–Figure 13 illustrates the percentage contribution of different driver groups to the total SHAP value across all studied watersheds for the 6-month prediction horizon.

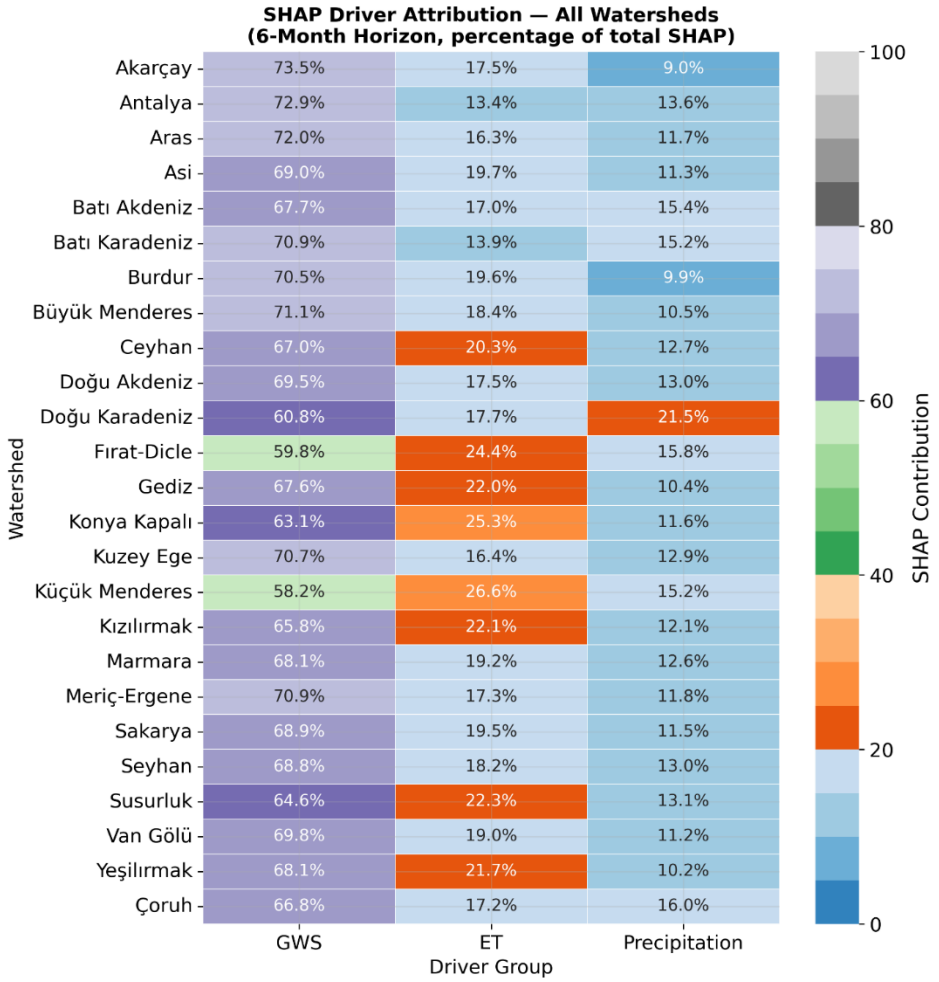


Figure 13. SHAP-based driver attribution across 25 river watersheds for the 6-month forecast horizon. Each cell shows the percentage contribution of a driver group (GWS, ET and precipitation) to the total absolute SHAP value for that watershed, summing to 100% across each row. Color intensity indicates the magnitude of SHAP contribution.

According to Figure 13, GWS history is the dominant driver group in all 25 watersheds, accounting for 58% (Küçük Menderes) to 74% (Akarçay) of the total absolute SHAP value (mean 68%). ET is the second most important group in 22 watersheds (13–27% overall; highest in Küçük Menderes, 26.6%, Konya Kapalı, 25.3%, and Fırat-Dicle, 24.4%), whereas precipitation is second in Antalya, Batı Karadeniz and Doğu Karadeniz (21.5% in Doğu Karadeniz, the largest precipitation share). Averaged over the watersheds, ET (19%) contributes more than precipitation (13%). The shares are similar among watersheds: the combined ET and precipitation share ranges only from 26% to 42%, so the model does not indicate a watershed-specific dominance of a single climatic driver.

Because the model predicts the change from the current anomaly, the dominance of GWS history reflects the strong autocorrelation of groundwater storage: the current state largely determines the state six months ahead. The ET and precipitation shares indicate which climatic

driver the model uses to modify this baseline, and ET rather than precipitation is used in most watersheds, consistent with the seasonal drawdown associated with increased ET described in Section 3.1.2.

3.4. GWS Criticality assessment and ranking

Figure 14 serves as the primary synthesis of this study's findings, showing the criticality ranking of the watersheds.

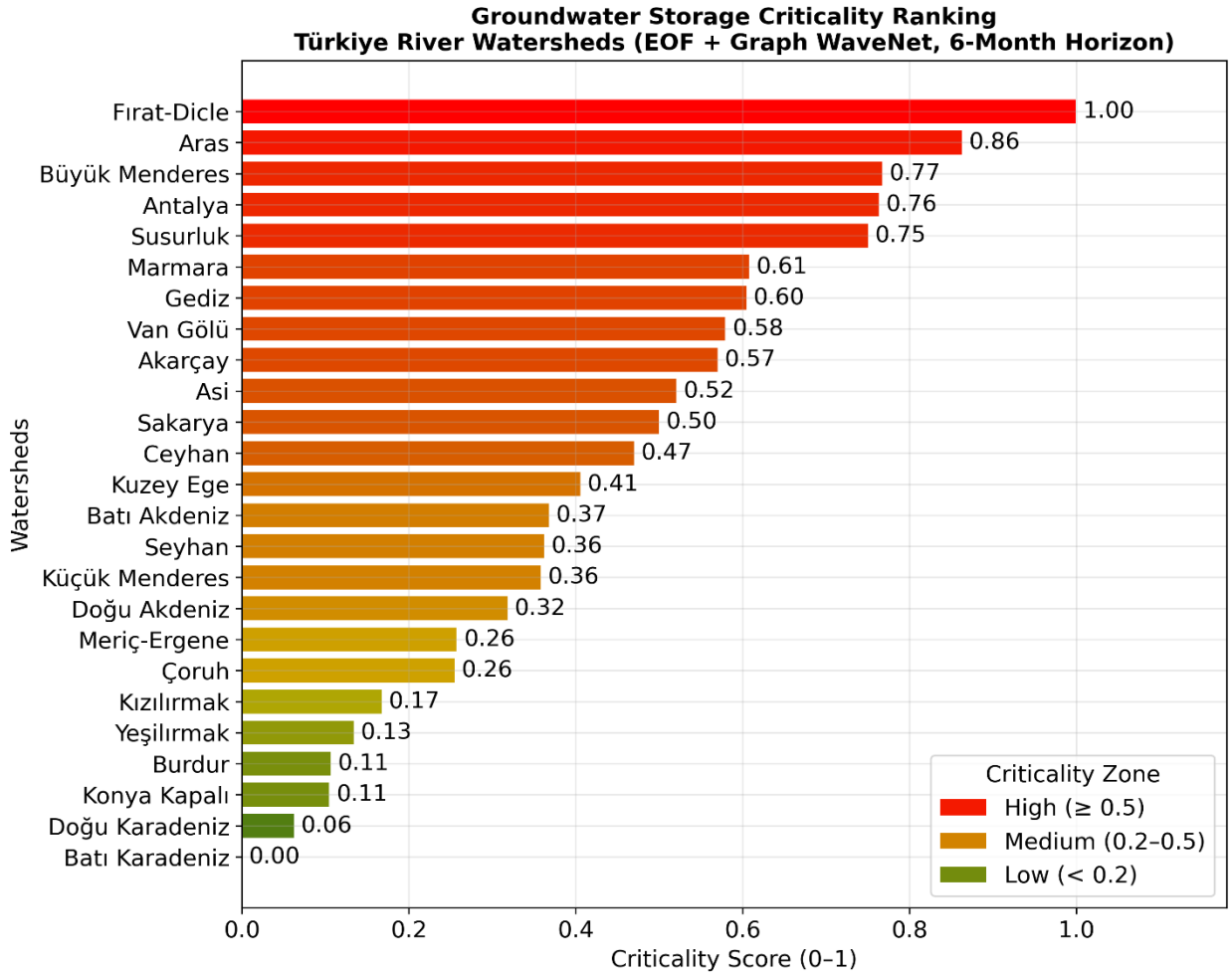


Figure 14. GWS criticality ranking for 25 watersheds, derived from a composite index integrating GWN 6-month predictions, GradientSHAP driver attribution, Mann-Kendall trend analysis, and watershed physical and demographic characteristics. Watersheds are ordered by descending criticality score (0–1). Color zones indicate high (≥0.5, red), medium (0.2–0.5, orange-yellow), and low (<0.2, green) criticality.

According to our results, Fırat-Dicle is the most critical watershed (score 1.00), followed by Aras (0.86), Büyük Menderes (0.77), Antalya (0.76) and Susurluk (0.75); Marmara, Gediz, Van Gölü, Akarçay and Asi (0.52–0.61) also exceed the 0.5 threshold, and Sakarya lies on it (0.50). The watersheds reach their scores through different components. Fırat-Dicle and Aras combine a

statistically significant depletion trend (−0.35 and −0.41 mm/month, $p < 0.001$) with a low GWS mean and a negative predicted anomaly. Van Gölü has a comparable trend (−0.42 mm/month) but a less negative predicted anomaly, which places it eighth. Büyük Menderes and Antalya rank high mainly because of large variability, deep historical minima and large seasonal amplitude, and Susurluk because of its predicted anomaly and trend acceleration, not because of a significant trend over the training period ($p = 0.93$, 0.41 and 0.69, respectively), and Marmara mainly because of the highest population density (785 persons/km²).

Fırat-Dicle and Aras are the two watersheds in which a significant depletion trend and a negative predicted anomaly coincide, and they are priority candidates for closer monitoring and further assessment. Since the score is a relative index, a high value indicates higher criticality compared with the other 24 watersheds, not an absolute level of risk. The sensitivity of the ranking to the assigned weights is examined in Section 3.5.

3.5 Sensitivity analysis of criticality scores

The individual influence of each index component has been further scrutinized through an OAT sensitivity analysis, as illustrated in Figure 15. In this analysis, each component's weight has varied from 0% to 200% of its baseline value, while others have been rescaled proportionally. As shown in Figure 15a, all sensitivity curves converge at the 100% baseline point (zero rank change). The 'Prediction' component (dark blue line) emerges as the most influential feature, exhibiting the steepest slope and reaching a mean absolute rank change of 2.0 when its weight is eliminated and 2.8 when it is doubled. Conversely, the 'GWS mean' (brown line), 'GWS minimum' (grey line) and 'GWS seasonal amplitude' (olive line) show low sensitivity (mean rank change ≤ 1.2), indicating that these secondary components contribute stably to the overall prioritization.

The stability of the ranking is further examined with Kendall's τ in Figure 15b. τ stayed above the 0.80 threshold for six of the nine components over the whole perturbation range. It fell below 0.80 for Prediction (to $\tau \approx 0.69$ when its weight is doubled), SHAP pressure (≈ 0.74 when removed) and GWS trend (≈ 0.75 at the extremes), i.e., for the three components that also dominate the rank changes. The first position is also sensitive to these weights: Fırat-Dicle remained top-ranked in all OAT scenarios for six of the nine components, whereas Aras overtook it when the Prediction weight was raised to $\geq 180\%$ of its baseline or the SHAP-pressure weight was reduced to $\leq 40\%$, and Antalya when the GWS-trend weight was reduced to $\leq 30\%$. The ranking is thus stable under moderate changes of most weights, but the identity of the single top-ranked watershed depends on the weights of these three components.

b)

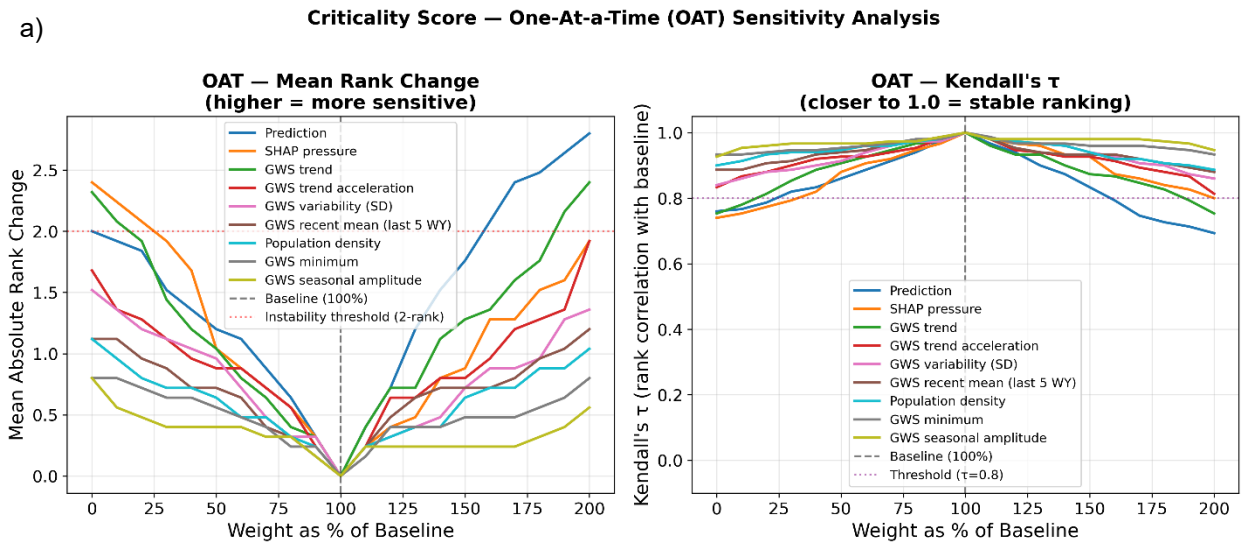


Figure 15. OAT sensitivity analysis. (a) Mean absolute rank change across all 25 watersheds when each component weight varies from 0 to 200% of its assigned value while others are rescaled proportionally. The red dotted line marks the 2-rank instability threshold. (b) Kendall's τ rank correlation between the baseline and perturbed rankings; values approaching 1.0 indicate stable rankings. The green dotted line marks τ = 0.80.

The sensitivity of the ranking was also examined with an MC analysis of 10,000 weight combinations. Figure 16 (a) shows the frequency with which each watershed is ranked as the most critical. Fırat-Dicle is ranked first in about 42% of the simulations ('consistently critical', P > 20%), followed by Aras (18%), Antalya (16%), Akarçay (12%) and Marmara (9%) ('sometimes critical', 5% < P < 20%); these five watersheds account for about 97% of the rank-1 outcomes. Figure 16 (b) shows the rank uncertainty over the 5th–95th percentile range. The five watersheds with the highest baseline scores (Fırat-Dicle, Aras, Büyük Menderes, Antalya, Susurluk) also have the lowest median ranks (2–5), and the bands of Fırat-Dicle, Aras, Büyük Menderes and Susurluk stay within ranks 1–11. The rank of several watersheds is much less certain (e.g., Antalya, Akarçay, Marmara, Küçük Menderes and Batı Akdeniz have bands spanning 16–22 positions). Because the Dirichlet sampling is concentrated around the expert weights (α = 10 w), these results indicate local sensitivity only.

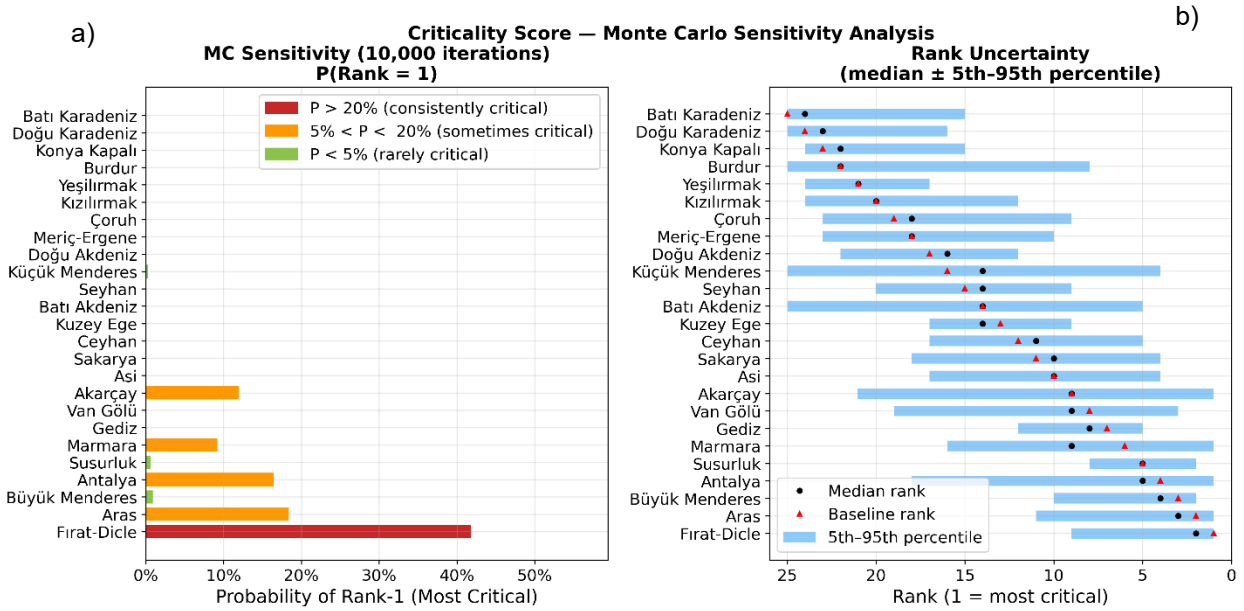


Figure 16. MC sensitivity analysis (n = 10000 iterations) of the criticality ranking. (a) Probability of each watershed achieving Rank-1 (most critical) across randomly sampled weight combinations drawn from a Dirichlet distribution. (b) Rank uncertainty shown as median (•) and 5th–95th percentile range for each watershed; narrow bands indicate that the rank is stable across the sampled weights.

Figure 17 shows the combined sensitivity results. In Figure 17 (a), Prediction (2.8), GWS trend (2.4) and SHAP pressure (2.4) exceed the 2-rank instability threshold and are the main contributors to ranking sensitivity; trend acceleration (1.9) and variability (1.5) lie below it, and the remaining four components (GWS mean, population density, seasonal amplitude and minimum; ≤ 1.2) have only a minor effect.

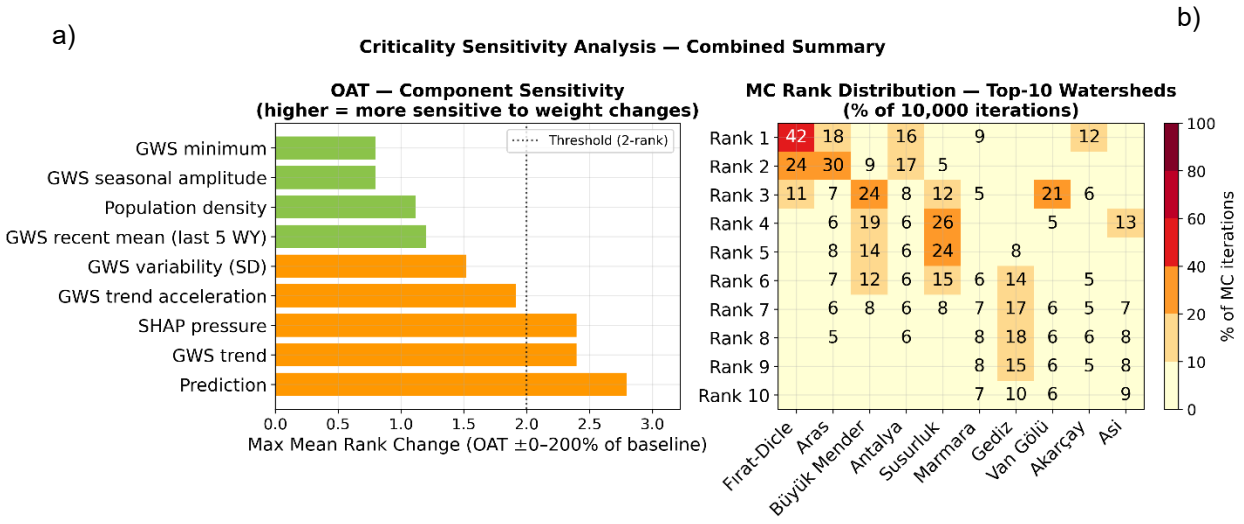


Figure 17. Combined sensitivity analysis results. (a) OAT sensitivity ranking shows the maximum mean rank change when each component weight is varied from 0% to 200% of its assigned value. (b) Heatmap showing MC rank distribution for the top 10 critical watersheds; cell values represent

the percentage of 10000 iterations in which each watershed has been assigned the corresponding rank.

The combined results reconcile the OAT and MC perspectives: the three components with the highest OAT sensitivity (Prediction, GWS trend and SHAP pressure) are those that decide between the leading candidates, and Fırat-Dicle, Aras and Antalya together capture about 76% of all rank-1 assignments in the MC simulation (Figure 17(b), top row). Overall, the results suggest that the set of highest-ranked watersheds is not an artifact of a single weighting scheme, whereas the first position depends on the weights of the prediction, SHAP and trend components.

4. Conclusion

This study presented an integrated, data-driven framework that combines dimensionality reduction (EOF), spatiotemporal deep learning (GWN), explainable artificial intelligence (GradientSHAP), and multi-criteria decision analysis to identify the most critical watersheds in terms of GWS among Türkiye's 25 major watersheds and the factors that dominate GWS variability in each of them, with the prediction model serving as the basis for the attribution.

The spatial and seasonal analyses revealed a clear and concerning signal: GWS conditions across Türkiye, as represented in the GLDAS-based GWS estimates, have deteriorated over the past two decades, with the dominance of positive anomalies during 2004–2014 WYs giving way to widespread negative anomalies during 2015–2024 WYs. This shift, observed consistently across all seasons and most pronounced in the central, eastern, and southeastern parts of the study area, indicates that groundwater depletion in Türkiye is no longer confined to isolated drought episodes but may reflect a structural, watershed-scale alteration of the hydrological regime. The substantial heterogeneity observed among watersheds—in trend magnitude, seasonal amplitude, and ~~recovery behavior~~ recovery behavior—further indicates that nationwide or regionally averaged assessments could obscure critical local dynamics, supporting the watershed-scale approach adopted here.

On the held-out five-year test period (October 2019 – September 2024), the GWN model reproduced the temporal pattern of GWS anomalies at the 6-month horizon (pooled $r = 0.75$) but overestimated their level (bias = +48 mm; NSE = −0.23, positive in 6 of 25 watersheds), because the predictions stay close to the training-period level, whereas the test period was drier than the training period. The model serves as the basis for the attribution analysis. The GradientSHAP analysis showed that GWS history dominates the model predictions in every watershed (58–74% of the total attribution), followed by ET (13–27%) and precipitation (9–22%), and that ET contributes more than precipitation in 22 of 25 watersheds. The similarity of the shares across watersheds indicates that the model does not single out a watershed-specific climatic driver; the attribution describes model behavior and not causal effects.

The central contribution of this work is the proposed criticality scoring framework, which moves beyond conventional trend-based assessments by fusing model predictions, SHAP-derived driver sensitivity, and historical GWS statistics into a single, interpretable index. This approach allows the framework to distinguish between watersheds that may exhibit superficially similar declining trends but differ in variability, seasonal amplitude, predicted anomaly, and demographic

exposure, a distinction that trend-only assessments do not provide. Applying this framework ranked Fırat-Dicle, Aras, Büyük Menderes, Antalya and Susurluk highest. The ranking is relative, and these watersheds reach their scores through different combinations of depletion trend, variability, and predicted anomaly (Section 3.4).

The Antalya watershed exhibits a pronounced vulnerability to hydro-climatic changes, characterized by statistically significant upward trends in both ambient temperatures and open-surface evaporation, alongside a concomitant decline in annual cumulative precipitation. Despite these increasingly arid conditions, expanding agricultural activities have driven a substantial rise in actively irrigated surface areas over time, placing severe stress on the regional water budget. When surface water availability falls short of demanding agricultural requirements, reliance heavily shifts toward groundwater resources. This intensive extraction is further exacerbated by the widespread proliferation of unauthorized and unregulated wells, which may contribute to depletion of the local aquifer. Consequently, over-abstraction in heavily cultivated zones has been reported to promote seawater intrusion along coastal margins, compromising the quality and sustainability of the watershed's vital freshwater resources (Ozcelik, 2022; Karatas et al., 2026). For Antalya, the ranking in Section 3.4 is driven mainly by variability, historical minimum and seasonal amplitude rather than by a significant GWS trend, so this context complements rather than explains the score.

Fırat-Dicle (Tigris-Euphrates) is a transboundary river basin that originates in the eastern part of Türkiye and extends through Syria and Iraq to the Persian Gulf (Kibaroglu, 2019). In this watershed, which is fed by snowmelt, many sectors contributing to the local economy in these countries include hydropower that produces electricity and operates agricultural irrigation systems, recreation, tourism activities (Kibaroglu, 2019), and supporting wildlife (Biricik et al., 2024). Hydroclimatic drivers and drought conditions are of great importance in groundwater depletion in this basin (Abdelmohsen et al., 2022; Chao et al., 2018).

The sensitivity of the prioritization to the weights was examined with OAT and MC analyses (10,000 weight scenarios). The five watersheds with the highest baseline scores keep the lowest median ranks under the perturbations considered, but the first position depends on the weights of the prediction, SHAP and trend components: Fırat-Dicle is ranked first in about 42% of the MC simulations and in all OAT scenarios except large changes of these three weights.

Taking the baseline score together with the MC results, ten watersheds stand out: Fırat-Dicle, Aras, Büyük Menderes, Antalya, Susurluk, Marmara, Gediz, Van Gölü, Akarçay and Asi (Table 7). Fırat-Dicle and Aras are distinguished by significant depletion trends combined with negative predicted anomalies; Büyük Menderes and Antalya by large variability, historical minima and seasonal amplitude, and Susurluk by its predicted anomaly and trend acceleration, each together with high SHAP pressure; and Marmara by its exceptionally high population density (approximately 19 million inhabitants), which raises its practical urgency independently of its hydrological signal. In all ten watersheds GWS memory is the dominant driver in the model (60–74%), followed by ET (13–24%) and precipitation (9–16%), so the SHAP analysis does not point

to a watershed-specific climatic cause of the criticality; attributing it to specific climatic or human factors requires additional data such as groundwater abstraction.

Table 7. Top 10 critical watersheds in Türkiye by baseline criticality score (Figure 14), with the probability of being ranked first in the MC analysis (Figure 16), the SHAP shares of GWS history, ET and precipitation (Figure 13) and the three highest-scoring normalized components.

Rank	Watershed	Score	MC P(Rank-1)* (%)	SHAP share GWS / ET / P (%)	Highest-scoring components
1	Fırat-Dicle	1.00	42	59.8 / 24.4 / 15.8	SHAP pressure, GWS trend, GWS mean
2	Aras	0.86	18	72.0 / 16.3 / 11.7	GWS mean, GWS trend, prediction
3	Büyük Menderes	0.77	<1	71.1 / 18.4 / 10.5	minimum, variability, SHAP pressure
4	Antalya	0.76	16	72.9 / 13.4 / 13.6	seasonal amplitude, variability, SHAP pressure
5	Susurluk	0.75	<1	64.6 / 22.3 / 13.1	prediction, trend acceleration, SHAP pressure
6	Marmara	0.61	9	68.1 / 19.2 / 12.7	population density, prediction, SHAP pressure
7	Gediz	0.60	0	67.6 / 22.0 / 10.4	variability, trend acceleration, minimum
8	Van Gölü	0.58	0	69.8 / 19.0 / 11.2	GWS trend, GWS mean, prediction
9	Akarçay	0.57	12	73.5 / 17.5 / 9.0	prediction, trend acceleration, minimum
10	Asi	0.52	0	69.0 / 19.7 / 11.3	GWS trend, GWS mean, seasonal amplitude

*MC P(Rank = 1): probability of each watershed achieving the top rank (Rank = 1) across 10000 MC weight perturbation iterations drawn from a Dirichlet distribution.

The results should be read within three bounds. First, the model reproduces the temporal pattern of GWS anomalies (r = 0.75) but overestimates their level (bias +48 mm at the 6-month horizon), so the SHAP attributions describe how the model reproduces the dynamics of GWS, not its level. Second, GWS history is an input of the model and dominates the attribution; a driver-only model (precipitation and ET) would be needed to isolate climatic effects. Third, the GWS estimates are a model–assimilation product and could not be validated against in-situ groundwater level observations, because spatially continuous and temporally consistent well-level records suitable for nationwide validation have not been available for this study, a limitation common in regional groundwater assessments (Famiglietti, 2014).

Future work should use emerging monitoring datasets to validate the satellite-derived anomalies and the criticality classes directly, add a driver-only model and groundwater abstraction, and quantify predictive uncertainty.

Within these bounds, the framework identifies Fırat-Dicle and Aras as the watersheds where a significant depletion trend and a negative predicted anomaly coincide, shows that GWS memory and ET, rather than precipitation, dominate the model's response, and, since it relies only on satellite-derived storage, climatic forcing and demographic data, may be applicable to other data-scarce regions.

Data Availability

All data used in this study is publicly available. GWS data can be found in https://disc.gsfc.nasa.gov/datasets/GLDAS_CLSM025_DA1_D_2.2/summary. ECMWF's ERA5-land hourly precipitation and AgERA5 potential evapotranspiration data can be found in https://doi.org/10.24381/cds.e2161bac and https://doi.org/10.24381/f9c1f09d, respectively. The number of district-level populations can be obtained through https://veriportali.tuik.gov.tr/en/databrowser/tuik/categories/11/11_1/11_1_1/TR,DF_ADNKS_T22,1.1.

References

Abdelmohsen, K., Sultan, M., Save, H., Abotalib, A. Z., Yan, E., & Zahran, K. H. (2022). Buffering the impacts of extreme climate variability in the highly engineered Tigris Euphrates river system. *Scientific Reports*, *12*(1), 4178. https://doi.org/10.1038/s41598-022-07891-0

Adam, M. A., Scheiber-Enslin, S. E., & Ali, K. A. (2026). Application of random forest modeling to evaluate groundwater storage changes in the Breede Water Management Area, South Africa. *Hydrogeology Journal*, 1-16. https://doi.org/10.1007/s10040-026-03047-w

Aeschbach-Hertig, W., & Gleeson, T. (2012). Regional strategies for the accelerating global problem of groundwater depletion. *Nature Geoscience*, *5*(12), 853-861. https://doi.org/10.1038/ngeo1617

Ahmadi, H., Kaya, O. A., Babadagi, E., Savas, T., & Pekkan, E. (2020). GIS-based groundwater potentiality mapping using AHP and FR models in central Antalya, Turkey. *Environmental Sciences Proceedings*, *5*(1), 11. https://doi.org/10.3390/IECG2020-08741

Aksoy, N., Şimşek, C., & Gunduz, O. (2009). Groundwater contamination mechanism in a geothermal field: a case study of Balcova, Turkey. *Journal of contaminant hydrology*, *103*(1-2), 13-28. https://doi.org/10.1016/j.jconhyd.2008.08.006

Baba, A., & Tayfur, G. (2011). Groundwater contamination and its effect on health in Turkey. *Environmental Monitoring and Assessment*, *183*(1), 77-94. https://doi.org/10.1007/s10661-011-1907-z

Baydaroğlu, Ö., & Demir, I. (2024). Temporal and spatial satellite data augmentation for deep learning-based rainfall nowcasting. *Journal of Hydroinformatics*, *26*(3), 589-607. https://doi.org/10.2166/hydro.2024.235

Baydaroğlu, Ö., Muste, M., Cikmaz, A. B., Kim, K., Meselhe, E., & Demir, I. (2024). Testing protocols for smoothing datasets of hydraulic variables acquired during unsteady flows. *Hydrological Sciences Journal*, *69*(13), 1813-1830. https://doi.org/10.1080/02626667.2024.2394169

Baydaroğlu, Ö., Yeşilköy, S., Dave, A., Linderman, M., & Demir, I. (2025). Modeling Algal Toxin Dynamics and Integrated Web Framework for Lakes. *Toxins*, *17*(7), 338. https://doi.org/10.3390/toxins17070338

Biricik, M., Safi, K., & Turğa, Ş. (2024). Remote Sensing Data Reveal a Significant Reduction in the Area of the Nesting Habitat of Rafetus euphraticus in the Tigris River, Southeastern Turkey. *Ecology and Evolution*, *14*(12), e70691. https://doi.org/10.1002/ece3.70691

Bozdağ, A., Ünal, Z., Karkınlı, A. E., Soomro, A. B., Mir, M. S., & Gulzar, Y. (2025). An Integrated Approach for Groundwater Potential Prediction Using Multi-Criteria and Heuristic Methods. *Water*, *17*(8), 1212. https://doi.org/10.3390/w17081212

Castillo, J. N., Resabala, V. F., Freire, L. O., & Corrales, B. P. (2022). Modeling and sensitivity analysis of the building energy consumption using the Monte Carlo method. *Energy Reports*, *8*, 518-524. https://doi.org/10.1016/j.egyr.2022.10.198

Chakraborty, D., Başağaoğlu, H., Gutierrez, L., & Mirchi, A. (2021). Explainable AI reveals new hydroclimatic insights for ecosystem-centric groundwater management. *Environmental Research Letters*, *16*(11), 114024. https://doi.org/10.1088/1748-9326/ac2fde

Chao, N., Luo, Z., Wang, Z., & Jin, T. (2018). Retrieving groundwater depletion and drought in the Tigris-Euphrates Basin between 2003 and 2015. *Groundwater*, *56*(5), 770-782. https://doi.org/10.1111/gwat.12611

Clark, S. R., Fu, G., & Janardhanan, S. (2025). Explainable AI for interpreting spatiotemporal groundwater predictions. *Water Resources Research*, *61*(10), e2025WR041303. https://doi.org/10.1029/2025WR041303

Cleveland, R. B., Cleveland, W. S., McRae, J. E., & Terpenning, I. (1990). STL: A seasonal-trend decomposition procedure based on loess. Journal of Official Statistics, 6(1), 3-73.

Conlin, M. P., Adams, P. N., Jaeger, J. M., & MacKenzie, R. (2020). Quantifying seasonal-to-interannual-scale storm impacts on morphology along a cuspate coast with a hybrid empirical orthogonal function approach. *Journal of Geophysical Research: Earth Surface*, *125*(12), e2020JF005617. https://doi.org/10.1029/2020JF005617

Davari, S., Eslamian, S., Jamali, M., & Safavi, H. R. (2025). Application of machine learning algorithms for groundwater level prediction in the Najafabad plain. *Scientific Reports, 16,* 2476. https://doi.org/10.1038/s41598-025-32376-1

Davraz, A., & Batur, B. (2021). Hydrogeochemistry characteristics of groundwater and health risk assessment in Yalvaç–Gelendost basin (Turkey). *Applied Water Science*, *11*(4), 67. https://doi.org/10.1007/s13201-021-01401-9

Demiray, B. Z., Mermer, O., Baydaroğlu, Ö., & Demir, I. (2025). Predicting harmful algal blooms using explainable deep learning models: A comparative study. *Water*, *17*(5), 676. https://doi.org/10.3390/w17050676

Demirci, M., Üneş, F., & Körlü, S. (2019). Modeling of groundwater level using artificial intelligence techniques: a case study of Reyhanli region in Turkey. *Applied Ecology & Environmental Research*, *17*(2). http://dx.doi.org/10.15666/aeer/1702_26512663

Dilcan, C. C., & Koksal, M. A. (2026). Basin-based evaluation of the water–energy–climate nexus in Türkiye: Climate scenarios-based ANFIS and GIS assessment. *Journal of Hydrology: Regional Studies*, *65*, 103477. https://doi.org/10.1016/j.ejrh.2026.103477

Di Lullo, G., Gemechu, E., Oni, A. O., & Kumar, A. (2020). Extending sensitivity analysis using regression to effectively disseminate life cycle assessment results. *The International Journal of Life Cycle Assessment*, *25*(2), 222-239. https://doi.org/10.1007/s11367-019-01674-y

Djessou, R. D., Wan, X., Yi, S., Annan, R. F., Su, X., & Wang, S. (2022). Water storage variation and its possible causes detected by GRACE in the Volta River Basin. *Remote Sensing*, *14*(21), 5319. https://doi.org/10.3390/rs14215319

Ertürk, A., Ekdal, A., Gürel, M., Karakaya, N., Guzel, C., & Gönenç, E. (2014). Evaluating the impact of climate change on groundwater resources in a small Mediterranean watershed. *Science of the total environment*, *499*, 437-447. https://doi.org/10.1016/j.scitotenv.2014.07.001

Famiglietti, J. S. (2014). *The global groundwater crisis, Nature Climate Change, 4(11), 945–948.* https://doi.org/10.1038/nclimate2425

Fraehr, N., Wang, Q. J., Wu, W., & Nathan, R. (2022). Upskilling low-fidelity hydrodynamic models of flood inundation through spatial analysis and Gaussian process learning. *Water Resources Research*, *58*(8), e2022WR032248. https://doi.org/10.1029/2022WR032248

Ge, H., & Asgarpoor, S. (2011). Parallel Monte Carlo simulation for reliability and cost evaluation of equipment and systems. *Electric power systems research*, *81*(2), 347-356. https://doi.org/10.1016/j.epsr.2010.09.012

Gleeson, T., Wada, Y., Bierkens, M. F., & Van Beek, L. P. (2012). Water balance of global aquifers revealed by groundwater footprint. *Nature*, *488*(7410), 197-200. https://doi.org/10.1038/nature11295

Güler, C., Kurt, M. A., Alpaslan, M., & Akbulut, C. (2012). Assessment of the impact of anthropogenic activities on the groundwater hydrology and chemistry in Tarsus coastal plain (Mersin, SE Turkey) using fuzzy clustering, multivariate statistics and GIS techniques. *Journal of Hydrology*, *414*, 435-451.

Gunduz, O., Simsek, C., & Hasozbek, A. (2010). Arsenic pollution in the groundwater of Simav Plain, Turkey: its impact on water quality and human health. *Water, air, and soil pollution*, *205*(1), 43-62.

Ham, Y. G., Kim, J. H., & Luo, J. J. (2019). Deep learning for multi-year ENSO forecasts. *Nature*, *573*(7775), 568-572.

Hannachi, A., Jolliffe, I. T., & Stephenson, D. B. (2007). Empirical orthogonal functions and related techniques in atmospheric science: A review. *International journal of climatology*, *27*(9), 1119-1152.

Helton, J. C. (1993). Uncertainty and sensitivity analysis techniques for use in performance assessment for radioactive waste disposal. *Reliability Engineering & System Safety*, *42*(2-3), 327-367.

Kara, H. (2025). The prediction of heavy metal contamination in groundwater using machine learning algorithms: a case study from the Harran Plain, a major agricultural irrigation area in Türkiye. *Environmental Geochemistry and Health*, *47*(8), 328.

Karatas, B. S., Cetinkaya, B., & Cengil, B. (2026). Spatial and temporal trend analysis of groundwater depth and salinity using geostatistics integrated with GIS in the Koprucay irrigation system in Antalya, Turkey. *Irrigation and Drainage*, *75*(1), 290-304.

Kavurmaci, M., & Üstün, A. K. (2016). Assessment of groundwater quality using DEA and AHP: a case study in the Sereflikochisar region in Turkey. *Environmental monitoring and assessment*, *188*(4), 258.

Kendall, M. G. (1975). Rank correlation methods (4th ed.). Charles Griffin.

Kibaroglu, A. (2019). State-of-the-art review of transboundary water governance in the Euphrates–Tigris river basin. *International Journal of Water Resources Development*, *35*(1), 4-29. https://doi.org/10.1080/07900627.2017.1408458

Kingma, D. P., & Ba, J. (2015). Adam: A method for stochastic optimization. International Conference on Learning Representations (ICLR). https://arxiv.org/abs/1412.6980

Kokhlikyan, N., Miglani, V., Martin, M., Wang, E., Alsallakh, B., Reynolds, J., ... & Reblitz-Richardson, O. (2020). Captum: A unified and generic model interpretability library for PyTorch. arXiv preprint arXiv:2009.07896.

Kuang, X., Liu, J., Scanlon, B. R., Jiao, J. J., Jasechko, S., Lancia, M., ... & Zheng, C. (2024). The changing nature of groundwater in the global water cycle. *Science*, *383*(6686), eadf0630. https://doi.org/10.1126/science.adf0630

Li, B., H. Beaudoing, and M. Rodell, NASA/GSFC/HSL (2020), GLDAS Catchment Land Surface Model L4 daily 0.25 x 0.25 degree GRACE-DA1 V2.2, Greenbelt, Maryland, USA, Goddard Earth Sciences Data and Information Services Center (GES DISC), Accessed: [*Last Accessed on June 29, 2026*], 10.5067/TXBMLX370XX8

Li, W., Bao, L., Yao, G., Wang, F., Guo, Q., Zhu, J., ... & Lu, S. (2024). The analysis on groundwater storage variations from GRACE/GRACE-FO in recent 20 years driven by influencing factors and prediction in Shandong Province, China. *Scientific Reports*, *14*(1), 5819.

Lorenz, E. N. (1956). *Empirical orthogonal functions and statistical weather prediction* (Vol. 1, p. 52). Cambridge: Massachusetts Institute of Technology, Department of Meteorology.

Loshchilov, I., & Hutter, F. (2017). SGDR: Stochastic gradient descent with warm restarts. International Conference on Learning Representations (ICLR). https://arxiv.org/abs/1608.03983

Lundberg, S. M., & Lee, S. I. (2017). A unified approach to interpreting model predictions. *Advances in neural information processing systems*, *30*.

Lundberg, S. M., Erion, G., Chen, H., DeGrave, A., Prutkin, J. M., Nair, B., ... & Lee, S. I. (2020). From local explanations to global understanding with explainable AI for trees. *Nature machine intelligence*, *2*(1), 56-67.

Mann, H. B. (1945). Nonparametric tests against trend. Econometrica, 13(3), 245-259.

Mermer, O., Liu, Y., Jennissen, C. A., Sonka, M., & Demir, I. (2026). Agricultural Injury Severity Prediction Using Integrated Data-Driven Analysis: Global Versus Local Explainability Using SHAP. *Safety*, *12*(1), 6.

Morris, M. D. (1991). Factorial sampling plans for preliminary computational experiments. *Technometrics*, *33*(2), 161-174.

Nas, B., & Berktay, A. (2006). Groundwater contamination by nitrates in the city of Konya,(Turkey): A GIS perspective. *Journal of Environmental management*, *79*(1), 30-37.

Owais, M., & Ramadan, I. (2025). Integrated Deep Learning and Global Sensitivity Analysis Framework for Transportation Link Criticality Evaluation. *Transportation Research Record*, 03611981251394975.

Ozdemir, A. (2011). Using a binary logistic regression method and GIS for evaluating and mapping the groundwater spring potential in the Sultan Mountains (Aksehir, Turkey). *Journal of Hydrology*, *405*(1-2), 123-136.

Ozcelik, M. (2022). Potential effects of excessive water withdrawal from boreholes drilled in the Antalya (Turkey) travertine plateau and well interactions. *Euro-Mediterranean Journal for Environmental Integration*, *7*(2), 241-249.

Raju, A., Singh, R. P., & Sinha, M. (2024, July). Predicting Change in Groundwater Storage Associated to Hydroclimatic Variability in the Indo-Gangetic Plains, India. In *IGARSS 2024-2024 IEEE International Geoscience and Remote Sensing Symposium* (pp. 389-392). IEEE.

Salih, A. M., Raisi-Estabragh, Z., Galazzo, I. B., Radeva, P., Petersen, S. E., Lekadir, K., & Menegaz, G. (2025). A perspective on explainable artificial intelligence methods: SHAP and LIME. *Advanced Intelligent Systems*, *7*(1), 2400304.

Saltelli, A., Ratto, M., Andres, T., Campolongo, F., Cariboni, J., Gatelli, D., Saisana, M., & Tarantola, S. (2008). Global sensitivity analysis: The primer. John Wiley & Sons.

Sen, P. K. (1968). Estimates of the regression coefficient based on Kendall's tau. Journal of the American Statistical Association, 63(324), 1379-1389.

Shamsudduha, M., Chandler, R. E., Taylor, R. G., & Ahmed, K. M. (2009). Recent trends in groundwater levels in a highly seasonal hydrological system: the Ganges-Brahmaputra-Meghna Delta. Hydrology and Earth System Sciences, 13(12), 2373-2385. https://doi.org/10.5194/hess-13-2373-2009

Shapley, L. S. (1953). A value for n-person games. Contributions to the Theory of Games, 2(28), 307-317.

Taşan, M. (2025). Improved prediction of groundwater quality index by hybrid machine learning models in a coastal region: A case study from Southern Turkey. *International Journal of Environmental Research*, *19*(4), 147.

Tayfur, G., Kirer, T., & Baba, A. (2008). Groundwater quality and hydrogeochemical properties of Torbalı Region, Izmir, Turkey. *Environmental Monitoring and Assessment*, *146*(1), 157-169.

Taylor, R. G., Scanlon, B., Döll, P., Rodell, M., Van Beek, R., Wada, Y., ... & Treidel, H. (2013). Ground water and climate change. *Nature climate change*, *3*(4), 322-329. https://doi.org/10.1038/nclimate1744

Tokatli, C., Köse, E., & Çiçek, A. (2013). Groundwater Quality of Türkmen Mountain, Turkey. *Polish Journal of Environmental Studies*, *22*(4).

Wang, B., Lee, J. Y., & Xiang, B. (2015). Asian summer monsoon rainfall predictability: a predictable mode analysis. *Climate Dynamics*, *44*(1), 61-74.

Wu, Z., Pan, S., Long, G., Jiang, J., & Zhang, C. (2019). Graph wavenet for deep spatial-temporal graph modeling. *arXiv preprint arXiv:1906.00121*.

Yazicigil, H., & Ekmekci, M. (2019). Groundwater. In *Water Resources of Turkey* (pp. 159-201). Cham: Springer International Publishing.

Yesilnacar, M. I., Sahinkaya, E., Naz, M., & Ozkaya, B. (2008). Neural network prediction of nitrate in groundwater of Harran Plain, Turkey. *Environmental Geology*, *56*(1), 19-25.

Yetiş, R., Atasoy, A. D., Demir Yetiş, A., & Yeşilnacar, M. İ. (2019). Hydrogeochemical characteristics and quality assessment of groundwater in Balikligol Basin, Sanliurfa, Turkey. *Environmental Earth Sciences*, *78*(11), 331.

Yeşilköy, S., Baydaroğlu, Ö., Singh, N., Sermet, Y., & Demir, I. (2024). A contemporary systematic review of cyberinfrastructure systems and applications for flood and drought data analytics and communication. *Environmental Research Communications*, *6*, 102003. https://doi.org/10.1088/2515-7620/ad85c4

Yeşilköy, S., & Baydaroğlu, Ö. (2025). Rain-on-snow climatology and its impact on flood risk in snow-dominated regions of Türkiye. *Theoretical and Applied Climatology*, *156*, 239. https://doi.org/10.1007/s00704-025-05463-6